Geochemistry, Geophysics, Geosystems®

RESEARCH ARTICLE
10.1029/2022GC010644

Special Section:
Insights into Subduction Zone Processes from Models and Observations of Exhumed Terranes

Metamorphism and Deformation on Subduction Interfaces: 1. Physical Framework

Philip C. England[1] **and Andrew J. Smye**[2]

[1]Department of Earth Sciences, University of Oxford, Oxford, UK, [2]Department of Geosciences, Pennsylvania State University, University Park, PA, USA

This article is a companion to Smye and England (2022), https://doi.org/10.1029/2022GC010645.

Key Points:

- A simple thermal and mechanical framework is presented for the interpretation of P-T data from high-pressure-low-temperature (HPLT) terrains
- PT data from HPLT terrains are consistent with thermal regimes of present-day plate interfaces (PI), with shear stresses of ~30–100 MPa
- Stresses are great enough that earthquakes can carry sediments to base of PI. Exhumation requires (near-)cessation of subduction

Correspondence to:
P. C. England,
philip.england@earth.ox.ac.uk

Citation:
England, P. C., & Smye, A. J. (2023). Metamorphism and deformation on subduction interfaces: 1. Physical framework. *Geochemistry, Geophysics, Geosystems*, *24*, e2022GC010644. https://doi.org/10.1029/2022GC010644

Received 3 AUG 2022
Accepted 4 OCT 2022

Author Contributions:
Conceptualization: Philip C. England, Andrew J. Smye
Formal analysis: Philip C. England, Andrew J. Smye
Investigation: Philip C. England, Andrew J. Smye
Methodology: Philip C. England, Andrew J. Smye

Abstract A thermal and mechanical framework is presented for analysis of pressure-temperature (P-T) data and structural observations from high-pressure-low-temperature (HPLT) terrains. P-T data from 281 HPLT rocks exhibit two regimes separated at a pressure of ~1.5 GPa, which corresponds to the modal maximum depth of thrust faulting in subduction zones. At pressures $\lesssim$1.5 GPa, interpreted as recording conditions on the plate interface, temperatures increase at about 350°C/GPa and are consistent with conditions calculated for shear stresses of ~30–100 MPa on the interface. Such shear stresses are high enough to carry several kilometers' thickness of sediment at least to the base of the plate interface. Burial of material on plate interfaces occurs predominantly during large-to-great earthquakes; the exhumation phase involves contrasts in ascent rates of adjacent units, because of their differing buoyancies and strengths. In consequence, juxtaposition of unrelated rock types is expected to be ubiquitous, during both descent and ascent. The scarcity of temperatures higher than ~650°C at pressures $\gtrsim$1.5 GPa may reflect loss of material from the wedge-slab interface by buoyant ascent. Exhumation of rocks in the subduction interface requires substantial reduction in shear stress, most plausibly by (near-)cessation of subduction. During prograde metamorphism temperatures increase smoothly with depth in the plate interface, with almost isothermal compression in the wedge-slab interface. Following cessation of subduction, rocks rising along the wedge-slab interface are likely to heat slightly during decompression. Within the plate interface, temperatures drop following the cessation of shear heating, and rocks follow counter-clockwise hairpin PT paths.

1. Introduction

Subduction zones host most of the Earth's great earthquakes and explosive volcanoes, and present one of the primary settings for chemical differentiation of the planet. Those processes are strongly influenced by the properties of the interface between the descending plate and the overriding plate and mantle wedge, often referred to as the subduction interface. For example, metamorphism of subducted hydrous slab-top rocks mediates global exchange of volatile elements between the hydrosphere and Earth's interior reservoirs (e.g., Bebout, 1995; Hacker, 2008; Kerrick & Connolly, 2001; Peacock, 1990; Rupke, 2004). Enrichment of primitive arc lavas in H_2O, large-ion lithophiles, and light rare earth elements implies appreciable mass transfer from the lower plate, across the subduction interface, to the arc wedge (e.g., Elliott et al., 1997; Hawkesworth et al., 1991, 1993; Plank & Langmuir, 1993; Tera et al., 1986; Turner & Langmuir, 2022). Seismic observations show that earthquakes in the upper 40–60 km of subduction zones, to perhaps as deep as 150 km, are located within low-wave-speed material that is often interpreted as representing the interface (e.g., Abers, 2005; Kim et al., 2012, 2014; Patzig et al., 2002; Song et al., 2009) implying that the generation of earthquakes, slow-slip events, and tremor in subduction zones depend on the physical properties of the subduction interface (e.g., Behr & Bürgmann, 2021; Saffer & Wallace, 2015).

Direct observations of active subduction interfaces are limited to depths of a few kilometers, but fragments of ocean-floor rocks containing metamorphic records of high pressure and low temperature (HPLT) are found widely in orogenic belts, and have commonly been considered to form on subduction interfaces (e.g., Ernst, 1971, 1973, 1975; Miyashiro, 1972, 1973; Oxburgh & Turcotte, 1971; Peacock, 1992). Recently, however, disagreement has arisen as to whether those terrains are representative of present-day subduction interfaces (e.g., Kohn et al., 2018; Peacock, 1992, 1996; Penniston-Dorland et al., 2015; Tsujimori & Ernst, 2013), or merely record conditions of generation or preservation that are unrelated to modern subduction interfaces (e.g., Abers et al., 2017; Syracuse et al., 2010; van Keken et al., 2018). A related matter is that geological observations from HPLT terrains are increasingly being used to propose detailed tectonic scenarios for their formation. Such

Validation: Philip C. England, Andrew J. Smye
Writing – original draft: Philip C. England, Andrew J. Smye
Writing – review & editing: Philip C. England, Andrew J. Smye

proposals are, however, often based on tenuous lines of argument, and contested among different authors. Investigation of these issues is hampered by the lack of a clear framework in which to interpret metamorphic data and observations.

Prerequisites for such a framework include that it be derived from the relevant physical equations, and that any geological outcome it predicts should be clearly connected to the physics behind those equations. The framework should also contain the essential features of the physical processes taking place in subduction zones, without incorporating so many complexities that clarity is lost. It is sometimes argued that simple models are not appropriate to geological processes, with complex models often being described as "realistic." That usage disguises pitfalls that are worth recalling in the present context. The greater the number of parameters a model has, the greater is the likelihood that it will fit the data that it was designed to fit, while nevertheless being incorrect (e.g., Ben-Zion, 2017; Dyson, 2004; Paola, 2011). Whereas any geological process might be complex in detail, it does not follow that any individual complex model lies close to reality. We therefore use models with few parameters. It is inevitable that a model with a small number of parameters will fail to fit all the details of a particular situation—a failure that could, but should not, be disguised by the addition of parameters. If, however, a simple model misfits the data in a range of situations, then we may be able to diagnose which of its assumptions is/are incorrect, and thereby develop our understanding of the processes.

This paper establishes a thermal and mechanical framework for the interpretation of the metamorphism and deformation of HPLT terrains. We use this framework to analyze the available P-T data and demonstrate that they are consistent with pressure-temperature conditions within present-day subduction zones that are constrained by heat flux measurements and seismological observations. We establish the conditions required for the generation and preservation of HPLT terrains, considering a wide range of rheological behavior and emphasizing the role of earthquakes in the burial process. We consider implications of this framework for the P-T-time (P-T-t) and P-T-deformation paths that rocks follow on the subduction interface. Section 2 describes the structural settings of HPLT terrains, and establishes a coherent set of pressure and temperature data from such terrains; these observations and data provide the constraints on our analyses. Section 3 sets out the thermal framework within which we analyze the P-T data and Section 4 uses it to test whether the data are consistent with pressure-temperature conditions within present-day subduction zones. We establish the mechanical framework in Section 5 and use it to discuss the conditions required for the generation and preservation of HPLT terrains, considering a wide range of rheological behavior and emphasizing the role of earthquakes in the burial process. Section 6 investigates the P-T-time (P-T-t) and P-T-deformation paths that rocks follow on the subduction interface. In a companion paper (Smye & England, 2022) we use this framework to calculate the mineral parageneses that would be generated for sedimentary and mafic rock types that are likely to be found on subduction interfaces, to constrain their rheological parameters and other physical properties, and to relate observations of HPLT terrains to processes occurring on present-day subduction interfaces.

2. Structural Settings and Metamorphic Data From HPLT Terrains

We assembled a set of 281 measurements of pressure and temperature from HPLT terrains regarded as having been metamorphosed within subduction interfaces. Appendix A explains how we assign uncertainties to the measurements; data and references are provided in Data Set 1 (https://doi.org/10.17605/OSF.IO/JASV5), available in the online data repository. This set of data overlaps with the compilations of Penniston-Dorland et al. (2015) and Agard et al. (2018) and includes data published more recently than, or that are otherwise not present in, previous compilations. This compilation also excludes some data present in other sets; our set is restricted to P-T estimates derived from subducted oceanic crust. We do not consider subducted continental crust, and we regard the data from locations referred to as "metamorphic soles to ophiolites" as being unrepresentative of HPLT rocks in general (see Figure 8b of Agard et al. [2018]).

2.1. Structural Settings of HPLT Terrains

Most of the P-T data come from rocks that are located in one or other of two tectonic settings. Of the 281 measurements, 231 are from structurally continuous slices, often referred to as thrust sheets, and 50 come from composite rock associations that are usually referred to as subduction mélanges.

2.1.1. HPLT Thrust Sheets

Thrust sheets of eclogite- and blueschist-facies rocks are dominated by clastic rocks that are interpreted as representing sediments derived either from the top of the lower plate or from the sedimentary apron to the forearc. Individual thrust sheets have a maximum thickness of ∼4 km and are generally <1 km thick (e.g., Agard et al., 2018; Kimura & Ludden, 1995). These thrust sheets commonly retain primary stratigraphic relations on length scales of meters to kilometers (e.g., Ernst, 1993; Kurz et al., 1998; Vitale Brovarone & Agard, 2013), and P-T estimates are usually similar within individual thrust sheets. Furthermore, geochronological data show that different structural levels within the same unit experienced similar P-T-t conditions (e.g., Agard et al., 2009; Guillot et al., 2009), implying that these slices behave coherently during both subduction and exhumation.

The thrust sheets often consist of a calcsilicate matrix containing centimetric to hectometric blocks of mafic oceanic rocks (e.g., England & Holland, 1979; O'Brien & Grove, 2022; Reinecke, 1998; Searle et al., 1994; Xia & Platt, 2017). Internal deformation fabrics include penetrative foliations, HP-mineral lineations and isoclinal folding of prograde or primary stratigraphic fabrics. Mafic rocks commonly occur as boudins within metasedimentary matrices with steep strain gradients proximal to boudin boundaries. The proportion of mafic rocks varies between localities but ultramafic bodies are rare, implying that the processes involved in formation and preservation of the thrust sheets take place within the subduction interface, and do not involve deeper portions of the lower plate, or upper mantle of the overriding plate and wedge.

HPLT thrust sheets are commonly bounded, above and below, by rocks of lower metamorphic grade and, in many cases, the upper boundary to the sheet is defined by a zone of normal-sense shear, whereas its base is defined by thrust-sense kinematic indicators (e.g., Maruyama et al., 1996; Platt, 1987). These associations are expected if such thrust sheets return to the surface under the influence of pressure gradients within a confined channel (e.g., England & Holland, 1979; Ernst et al., 1997; Platt, 1987, and see Section 5.5).

2.1.2. Blocks in Mélanges

The second common type of unit that is interpreted to represent part of the subduction interface consists of chaotic associations of blocks of eclogites and blueschists within intensely deformed matrices, which are dominated either by serpentinite-group minerals (35/50 samples), by low-grade mudrocks (14/50), or by both (8/50) (proportions of matrix lithologies taken from literature; see Data Set 1 [https://doi.org/10.17605/OSF.IO/JASV5]). Mafic eclogite and blueschist blocks within mélanges typically exhibit penetrative foliations defined by high-pressure phases and range in size from centimeters to hectometers; metasedimentary blocks are rare. Individual blocks typically have similar compositions to oceanic crust (e.g., Coleman et al., 1965, and references therein), record heterogeneous and diachronous metamorphic evolutions and yield distinct P-T-t paths in which the timing and conditions of HP metamorphism vary non-systematically with structural depth in the terrain. In our compilation, we report the P-T conditions recorded by the blocks, not those of the matrices. The densities of serpentinites are low compared both with the blocks they enclose, and with the plates and mantle surrounding the interface (∼2.5–2.8 Mg m^{-3}, e.g., Christensen, 2004; Coleman, 1971), so it is reasonable to envisage that serpentinite mélanges represent the ascent of buoyant material within the subduction interface (England & Holland, 1979; Hermann et al., 2000) in a fashion similar to, but less coherent than, the thrust sheets (Section 5.5).

The smaller group of mélanges, in which the matrices consist of (meta-)sedimentary rocks, is dominated by samples from the Franciscan terrain of California, which has been the object of intense (and perhaps disproportionate) attention. The mechanics of emplacement of the Franciscan mélange must differ from that of the serpentinite mélanges and metasedimentary mélanges in Iran (Rad et al., 2005), Taiwan (Keyser et al., 2016) and Turkey (Şengün et al., 2012), because the matrix lithologies have experienced only low-grade metamorphism relative to entrained HP blocks (≲1 GPa and ≲300°C, Cloos, 1983; Ukar & Cloos, 2013). It is therefore probable that the blocks are derived from other HPLT units that were previously brought to the surface and dismembered before being incorporated into the shallow levels of the Franciscan subduction zone (Krohe, 2017; Platt, 2015; Wakabayashi, 2012; Wakabayashi & Dilek, 2011). Accordingly, we have restricted our analysis to mélange terrains in which it is demonstrated that the matrix materials underwent subduction-related HP metamorphism.

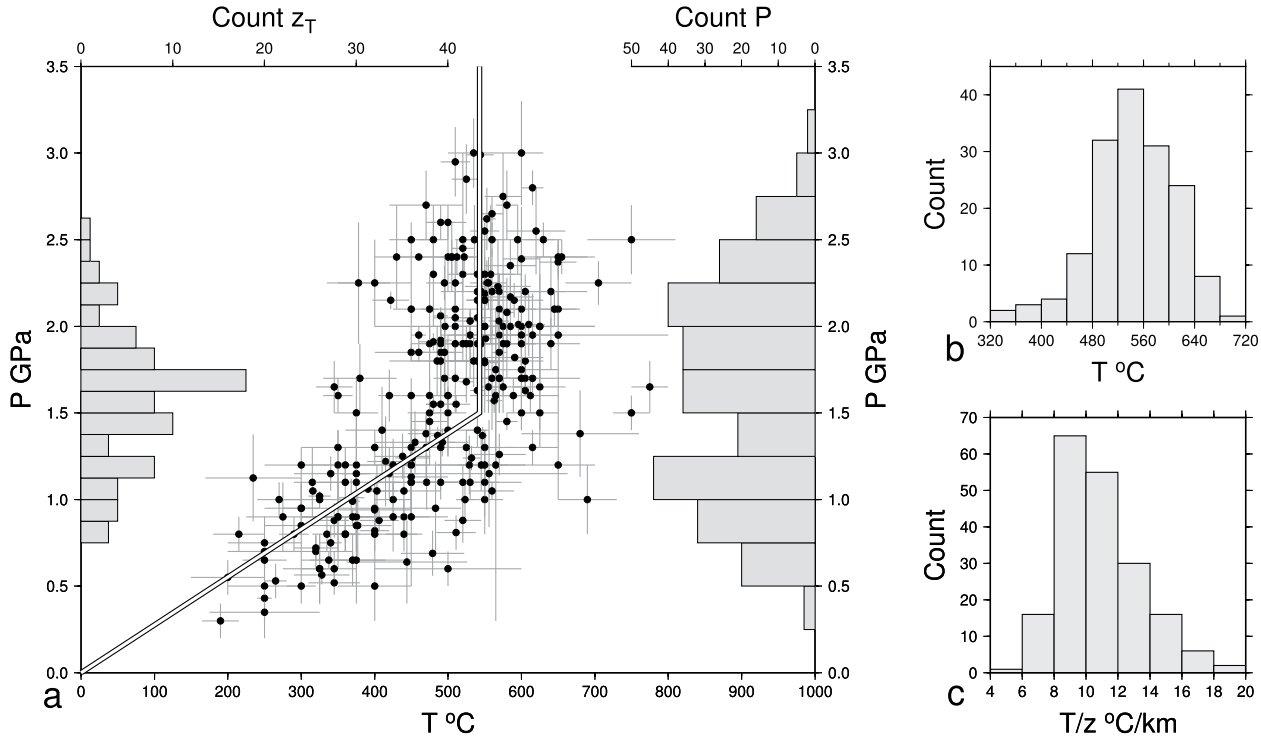

Figure 1. The 281 measurements of pressure and temperature from high-pressure-low-temperature terrains discussed in this paper (see Appendix A and Data Set 1 [https://doi.org/10.17605/OSF.IO/JASV5]) (a) P-T data, with 2-σ uncertainties shown by bars. Histogram (horizontal bars, right) shows distributions of pressures of the 281 measurements. Horizontal bars at the left show the distribution of maximum depth of thrust-faulting earthquakes, z_T, for 82 profiles across subduction zones (England, 2018) with depths are converted to pressure using PREM (Dziewonski & Anderson, 1981). (b) Scatter of temperatures for $P > 1.5$ GPa. (c) Distribution of P-T data from shallower than 1.5 GPa, expressed as apparent temperature gradients.

2.2. Pressure-Temperature Measurements

As do Penniston-Dorland et al. (2015), we include only P-T estimates derived from maximum pressure conditions. Generally, those estimates also correspond to maximum temperatures (e.g., Angiboust et al., 2012; Reinecke, 1991; Smye et al., 2011), although there are cases in which maximum temperatures occurred during decompression (e.g., Whitney & Davis, 2006) (see Appendix A).

The P-T estimates are derived from a range of different thermobarometric methods, including: pseudo-section analysis, conventional geothermobarometry, optimal thermobarometry (average P-T), single-phase solution thermometry, Raman barometry/thermometry and petrogenetic grids. Where available, P-T uncertainties for individual data points were taken from the literature cited in Data Set 1 (https://doi.org/10.17605/OSF.IO/JASV5). For P-T determinations by analysis of pseudo-sections and petrogenetic grids, uncertainties were determined by the P and T interval of the P-T stability field containing the peak pressure mineral assemblage. Where formal uncertainties were not provided we assumed nominal uncertainties of ±0.2 GPa in pressure and ±80°C in temperature (1-σ). Justification for these assumptions is presented in Appendix A; it is sufficient to note here that P-T estimates made by the two most commonly employed methods (pseudo-sections and average P-T method) exhibit distributions that are indistinguishable from one another (Figure A2).

The P-T data are shown in Figure 1a. At $P < 1.5$ GPa, temperatures increase by about 350°C per GPa. With T/P converted to apparent temperature gradient, 70% of the observations lie in the range 11 ± 3°C/km (Figure 1c). Such apparent temperature gradients are commonly regarded as being typical, or indeed diagnostic, of metamorphism in subduction zones (e.g., Agard et al., 2018, 2009; Bebout & Penniston-Dorland, 2016; Guillot et al., 2009; Kohn et al., 2018; Penniston-Dorland et al., 2015). They do not, however, persist to pressures greater than ~1.5 GPa; there, the temperatures are better described by a range of 560 ± 80°C that is independent of pressure (Figure 1b). These relations are summarized by the double line in Figure 1a. The transition between P-T gradients of ~350°C per GPa shallower than ~1.5 GPa and the smaller variations in temperature at greater pressure takes place over

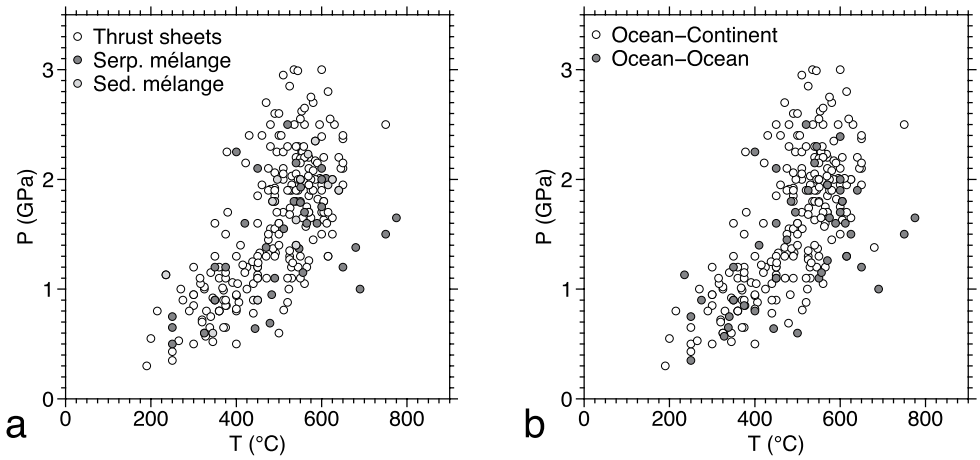

Figure 2. Data of Figure 1 separated according to structural setting and type of subduction zone. (a) P-T data plotted with open, dark gray, and light gray symbols, according to structural setting: high-pressure-low-temperature (HPLT) thrust sheets, HPLT blocks within a serpentinite or metasedimentary matrix, respectively. Uncertainties, shown in Figure 1, are omitted here for clarity. (b) P-T data for ocean-continent subduction zones are shown by open symbols; data from ocean-ocean zones are shown by gray symbols.

the range of the maximum depths of thrust-faulting earthquakes in present-day subduction zones (England, 2018; Hayes et al., 2018): see the histogram of those depths on the left of Figure 1a.

Agard et al. (2018) suggested that there are two peaks in the abundance of pressure recorded by HPLT rocks "at 30–40 km (i.e., down-dip of the seismogenic zone [sic]) and at 80 ± 10 km, perhaps with one additional peak at 50–55 km" and attributed a gap in return of rocks between 40 and 80 km to lubrication of the plate interface by serpentinite. Our compilation gives little support for that suggestion. The histogram to the right of Figure 1a shows the distribution of pressure data, with the width of the bins being 0.25 GPa, comparable with the uncertainties in pressure. Recorded pressures are approximately evenly distributed between about 0.75 and 2.5 GPa.

It has been suggested that systematic differences exist between P-T data from different structural settings (e.g., Agard et al., 2009, 2018; Guillot et al., 2009). In Figure 2a each P-T estimate is assigned to one of three structural classifications, based on the criteria presented in Sections 2.1.1 and 2.1.2: (a) HPLT thrust sheets, (b) HPLT blocks within a serpentinite or (c) metasedimentary matrix. The distribution of P-T estimates from HPLT thrust sheets is similar to that from exotic blocks within serpentinite and metasedimentary mélanges (Figure 2a). This observation disagrees with the contention of Guillot et al. (2009) and Agard et al. (2018) that exotic blocks within mélange preserve peak conditions that are systematically hotter than coherent slices, or thrust sheets. Maximum pressures are ∼2.5 GPa for blocks within mélanges and ∼3 GPa for thrust sheets. We have also assessed, from the original publications, whether the upper plate to the terrains is continental or oceanic. Figure 2b shows no discernible difference between the P-T conditions preserved from HPLT rocks from the two different types of subduction zone.

3. Thermal Framework

3.1. Configuration of the Subduction Interface

This paper is concerned with the conditions of pressure, temperature, and deviatoric stress in ocean-floor rocks during subduction and exhumation. The subduction interface contains two well-defined segments separated by a transitional region that is less well defined (Figure 3). The plate interface is the segment bounded by two rigid plates; the wedge-slab interface is the segment bounded by the descending lower plate and the mantle wedge. We avoid the term "subduction channel," which is often employed in this context, because it is sometimes applied to the plate interface alone, and sometimes to the whole interface.

The plate interface accommodates all the relative motion between the plates whereas, it is commonly assumed, the base of the mantle wedge moves with the same velocity as the slab, and the relative motion between the two plates is accommodated by flow in the wedge. The width of the transition between the two regimes is uncertain. It is

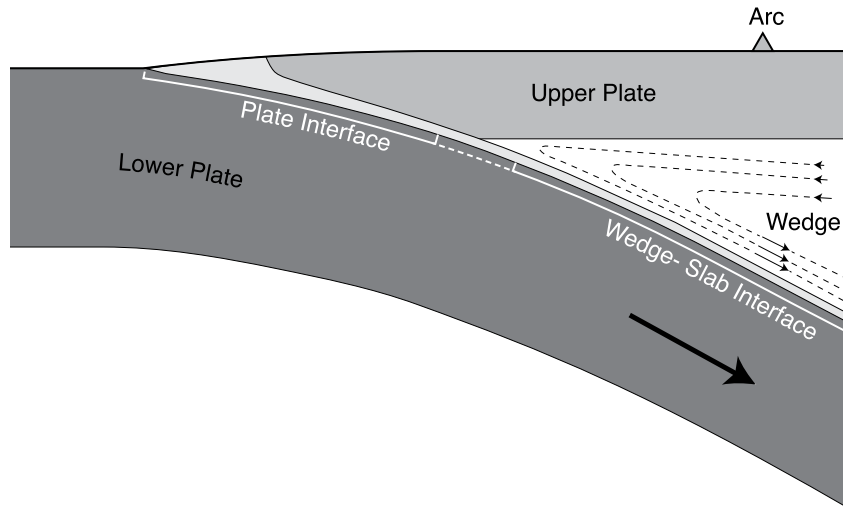

Figure 3. Definition sketch for the subduction interface. Material of the interface is shown in light gray, and the extents of plate and wedge-slab interfaces are indicated by the lines and labels beneath the interface. The transition between the two regimes is shown as a dashed line.

reasonable to assume that the plate interface extends at least to the maximum depth of thrust-faulting earthquakes, which varies from less than 30 km to more than 60 km from one subduction zone to another (England, 2018; Hayes et al., 2012, 2018; Heuret et al., 2011). The hypocenters, and in some cases the moment tensors, of low-frequency earthquakes and episodic tremor and slip (ETS) show that the plate interface extends beyond the maximum depth of thrust faulting earthquakes (e.g., Audet & Kim, 2016; Brown et al., 2009, 2013; Brudzinski et al., 2016; Ide & Yabe, 2014; Maury et al., 2016; Wech, 2021). Where the locations of ETS are well constrained, they are distributed over a depth range of approximately 10 km (e.g., Wech, 2021), but it is uncertain whether the plate boundary continues deeper than that. It has been suggested that zones of ETS are located close to the corner of the mantle wedge, although opinions differ as to whether they lie beneath the nose of the mantle wedge (e.g., Kato et al., 2010; Obara, 2011), are shallower than the nose (e.g., Audet et al., 2009; Peng & Gomberg, 2010), or straddle it (e.g., Wang & Tréhu, 2016).

Other lines of evidence, such as distributions of surface heat flux and attenuation of seismic waves, are less direct and do not constrain more tightly the depth of the transition. Wada and Wang (2009) investigated the constraints provided by measurements of surface heat flux, modeling the surface heat flux on 17 profiles across subduction zones. For three of these profiles, they showed that the heat flux data permit transitions in the depth range ~60–90 km (Wada & Wang, 2009, Figures 5–7). For the remaining 14 profiles they showed that a depth of 75 km is not inconsistent with the data (Wada & Wang, 2009, Figures 11 and A1–A13), although on most profiles the location of the transition is constrained by fewer than five data—sometimes none—and all permit a wide range of depth for the transition.

Zones of high seismic attenuation have been identified above the descending plate in a number of subduction zones (e.g., Chen & Clayton, 2009; Eberhart-Phillips et al., 2020; Kita et al., 2014; Liu et al., 2014; Nakajima et al., 2013; Rychert et al., 2008; Schurr et al., 2003, 2006; Stachnik et al., 2004; Ventouzi et al., 2018; Wei & Wiens, 2018). Many of those studies show a boundary between low and high attenuation in the wedge which, it is reasonable to assume, marks a change in properties of the wedge related to its thermal structure. If it is further assumed that this boundary marks the limit of that part of the wedge in which advection of heat dominates over diffusion, then the top of the slab beneath that boundary must be part of the wedge-slab interface—otherwise the slab would not be driving the flow necessary to advect that heat (e.g., Abers et al., 2020). Constraints from these data are also loose, because of the number of steps, and their uncertainties, in the chain of logic between measurement of attenuation and deduction of the depth of the base of the transition from plate to wedge-slab interface.

Because of these uncertainties, and because speculative models do not lead to reliable knowledge, we do not carry out calculations for the region of transition between the plate and wedge-slab interfaces. In this paper, and its companion (Smye & England, 2022), we concentrate on the upper 150 km of the subduction interface.

If the inferences of location of the wedge corner from ETS are correct, then the transition occupies about 10% of this interval; if, as hypothesized by Wada and Wang (2009), the depth of the wedge corner is a constant 75 km then that percentage may be somewhat larger on interfaces where the maximum depth of thrust faulting is shallower than 50 km.

3.2. Temperature Profiles

3.2.1. Plate Interface

We assume (following e.g., Molnar & England, 1990; Turcotte & Schubert, 1973), that the transport of heat at plate interfaces occurs principally by diffusion perpendicular to the interface and by advection parallel to the interface due to the relative motion of the two plates. We neglect any transport of heat along the interface by volatiles or by upward motion of interface material with respect to Earth's surface. This assumption allows us to use analytical expressions for temperature on the plate interface. van Keken et al. (2019) argued that analytical expressions are inaccurate when applied to curved plate interfaces, or when the ocean floor of the lower plate is young, but their arguments are erroneous (England & May, 2021, Section 2.4.1).

Dips, convergence rates, and ages of ocean lithosphere in ancient subduction zones are unknown; we therefore simplify the expressions of England and May (2021) by removing details that cannot be constrained. We approximate the cosine of the dip of the interface to one, neglect obliquity in convergence, and treat thermal properties as being constant. Temperatures on the plate interface, T_f, are then given by

$$T_f \approx \frac{Q z_f}{K S_Q} + \frac{\tau' V z_f}{K S_\tau}, \tag{1}$$

$$S_Q = 1 + b_Q \sqrt{\frac{V z_f^2}{\kappa u}}, \tag{2}$$

$$S_\tau = 1 + b_\tau \sqrt{\frac{V z_f^2}{\kappa u}}. \tag{3}$$

Here, z_f is the depth of the interface, u is the distance along the plate interface from the trench to point of interest, V is the convergence rate between the two plates, K is thermal conductivity, and κ is thermal diffusivity. Dissipative heating takes place at a rate $\tau' V$, where τ' is the average shear stress during relative motion across the interface; if that motion takes place primarily in earthquakes, then τ' may be much lower than the static shear stress (e.g., Rice, 2006).

The constants b_Q, b_τ are of order 1 (Table 1) and depend on the evolution of the temperature on the interface with time which, in turn, depends on the mode of heating and the shape of the interface (Molnar & England, 1990, Appendix B and England & May, 2021, Section 2.3). The lower plate is assumed to consist of ocean lithosphere of a given age as it passes beneath the point of interest (u, z_f); Q is the heat flux that would have been flowing through the surface of that lithosphere, had it not been subducted (for which we use the expressions of Parsons and Sclater [1977]).

The approximation sign in Equation 1 indicates that the analytical expressions agree with numerical solutions to the full equations within a few per cent, or a few tens of degrees (England & May, 2021; Molnar & England, 1990). The first term on the right-hand side gives the contribution to temperature on the interface from heat flowing out of the top of the lower plate; the second is the contribution from heating on the interface. Equation 1 shows that temperatures on the interface are reduced, by the divisor S_Q or S_τ, from those that would be calculated for the same sources of heat (Q and/or $\tau' V$), but in the absence of slip across the interface (England & May, 2021; Section 2.4; Molnar & England, 1990). The term in the square root of the divisor has the form of a Péclet number

$$\mathrm{Pe} = \frac{V z_f^2}{\kappa u} \tag{4}$$

Table 1
Notation and Values of Parameters

Parameter	Definition	Units or value
b_Q	$2/\sqrt{\pi}$ (Equation 2)[a]	
b_τ	$15\sqrt{\pi}/16$, $\tau' \propto z_f$ (Equation 3)[a]; $\sqrt{\pi}/2$, τ' constant[b]	
C	Rheological parameter (Equation C5 and C6)	Pa $s^{1/n}$
c	Curvature of the plate interface	1.5×10^{-3} km^{-1}
E	Activation energy for creep process	kJ/mol
g	Acceleration due to gravity	9.8 m s^{-2}
h	Thickness of subduction interface	m
K	Thermal conductivity	3 W m^{-1} K^{-1}
n	Power-law exponent for creep process	
Q	Surface heat flux appropriate to age of lower plate	mW m^{-2}
r	Radial distance from the corner of the mantle wedge	m
S_Q, S_τ	Divisors expressing influence of advection (Equations 2 and 3)	
t	Time	s
T[c]	Temperature	°C
T_f[c]	Temperature on the plate interface at depth z_f	Equation 1
T_T[c]	Temperature on the plate interface at depth z_T	
u, u_T	Distance along the subduction interface, measured from the trench	km
V	Speed of convergence between plates	mm/year
v	Speed, relative to upper plate, of material within the subduction interface	m
x_T	Horizontal distance from trench to point on surface above z_T	m
y	Distance measured perpendicular to surface of lower plate	m
z	Depth below surface	m
z_f	Depth of subduction interface	m
z_T	Maximum depth of thrust-faulting earthquakes on subduction interface	m
α	Thickness of advective-diffusive boundary layer at base of mantle wedge	Equation 7
β	Thickness of diffusive thermal boundary layer at top of lower plate	Equation 8
δ	Average dip of interface between surface and z_f	
$\dot{\varepsilon}$	Strain rate	s^{-1}
η	Viscosity	Pa s
Θ	Absolute temperature	K
$\kappa = \frac{K}{\rho c}$	Thermal diffusivity	10^{-6} m^2 s^{-1}
μ'	Effective coefficient of friction	Equation 5
ρ	Average density of the upper plate	kg m^{-3}
τ	Shear stress	Pa
τ'	Average shear stress during slip on plate interface	Pa Equation 1
Φ	Pressure gradient along the interface (Equation 15)	Pa m^{-1}

Note. Symbols used only in the Appendices, or only close to where they are defined, are omitted from this table.
[a]England and May (2021, Section 2.3). [b]Molnar and England (1990, p. 4839). [c]The Celsius scale is used; the boundary condition on temperatures at $z = 0$ (the land surface or the sea floor) is close to 0°C.

which is the ratio of the time scale for diffusion of heat through the thickness z_f of the upper plate, $\left(z_f^2/\kappa\right)$, to the time, u/V, taken for the lower plate to travel the distance u down the interface (England & May, 2021).

We consider two conditions for the shear stress, τ': in one it is constant along the plate interface and in the other it is proportional to depth

$$\tau' = \mu' g \rho z_f \tag{5}$$

where g is the acceleration due to gravity and ρ is the average density of the plate above z_f. Here μ' is an effective coefficient of friction; on most plate interfaces it represents heating in earthquakes and is not directly related to static friction (e.g., Kanamori & Rivera, 2006; Rice, 2006). As discussed in Section 3.1, we do not calculate temperatures in the transition region from the base of the plate interface to the wedge-slab interface because the magnitude of τ' is highly uncertain there.

The temperature gradient immediately beneath the interface is

$$\left.\frac{\partial T}{\partial y}\right|_{z_f -} \sim \frac{Q}{K} - \frac{T_f}{\sqrt{\kappa t}}, \tag{6}$$

where $t = u/V$ is the time taken for the top of the lower plate to pass from the trench to the point of interest and y is distance perpendicular to the interface (England & May, 2021; Molnar & England, 1990).

3.2.2. Wedge-Slab Interface

There is no analytical solution for temperature profiles along the wedge-slab interface, and numerical solutions differ considerably one from another because of differing assumptions about the nature and depth of the transition between plate and wedge-slab interfaces. Three specific aspects of the numerical solutions are robust, however, and these are central to the interpretation of P-T data from HPLT terrains.

The first aspect is an appreciable inverted temperature gradient that is developed over a distance $\sqrt{\kappa t}$ below the top of the lower plate (see Equation 6). By the time the lower plate reaches the top of the wedge-slab interface, 100–300 km from the trench at convergence rates of 30–100 mm/yr (see Figure 6, below), that distance is ~5–15 km. Second, temperature gradients along the wedge-slab interface are generally low (about 5°C per kilometer of depth), and are relatively insensitive to descent speeds and to age of the slab, provided that the age is more than about 25 My (e.g., England & Katz, 2010; England & Wilkins, 2004; Syracuse et al., 2010). The third aspect is that the temperature on the wedge-slab interface is controlled primarily by the maximum temperature in the wedge above it and, again, is insensitive to the parameters of subduction.

A scaling argument allows us to understand the insensitivity of temperature profiles along the wedge-slab interface to the parameters of subduction. Temperatures on the wedge-slab interface are controlled by a balance between advection of heat toward the top of the slab by the circulation in the wedge and diffusion perpendicular to the interface. A diffusive-advective boundary layer forms along the base of the wedge whose thickness, for a Newtonian wedge, scales as

$$\alpha \sim \left(\frac{\kappa r^2 \delta}{V}\right)^{\frac{1}{3}}, \tag{7}$$

where r is distance from the wedge corner (England & Wilkins, 2004). The inverted thermal gradient at the top of the lower plate is developed over a thickness,

$$\beta \sim \sqrt{\kappa t} \sim \sqrt{\frac{\kappa u}{V}} \tag{8}$$

(Equation 6). Writing T_w for the temperature in the interior of the wedge, at the top of the advective-diffusive boundary layer, and equating the thermal gradients above and below the wedge-slab interface

$$\frac{T_w - T_f}{\alpha} \sim \frac{T_f}{\beta} \tag{9}$$

$$\frac{T_f}{T_w} \sim \frac{1}{1 + \frac{\alpha}{\beta}} \tag{10}$$

The length scales α and β both increase with depth and decrease with convergence speed V; their ratio depends weakly on either parameter hence the temperature on the wedge-slab interface is close to a constant fraction of the maximum temperature in the wedge. For the range of conditions of relevance here, α and β are of comparable magnitude, so that fraction is approximately one half.

Although the scaling argument of Equations 7–10 was initially developed for the case in which the mantle wedge is a constant-viscosity fluid (England & Wilkins, 2004), England and Katz (2010, Figure 2 and Supplementary Information) showed that a similar scaling explains the dependence of T_f on T_w for their calculations, which used the rheological parameters for diffusion creep of olivine, and set the subduction interface to have constant dip with transition to the wedge-slab interface occurring at a depth of 55 km. Syracuse et al. (2010) calculated temperatures for 56 profiles across present-day subduction zones, using the observed configurations of plate interface for those zones, employing a combination of diffusion and dislocation creep parameters for the mantle (Karato & Wu, 1993). They allowed the transition to begin at a depth of 40–50 km. In one set of experiments the transition ends when a temperature of 550°C is reached on the interface; in a second set the transition ends at a depth of 80 km. Figure 4 shows that, in each of these sets of calculations, that ratio of T_f to T_w, for the great majority of calculations, lies within the range 0.5–0.65, consistent with the scaling argument above.

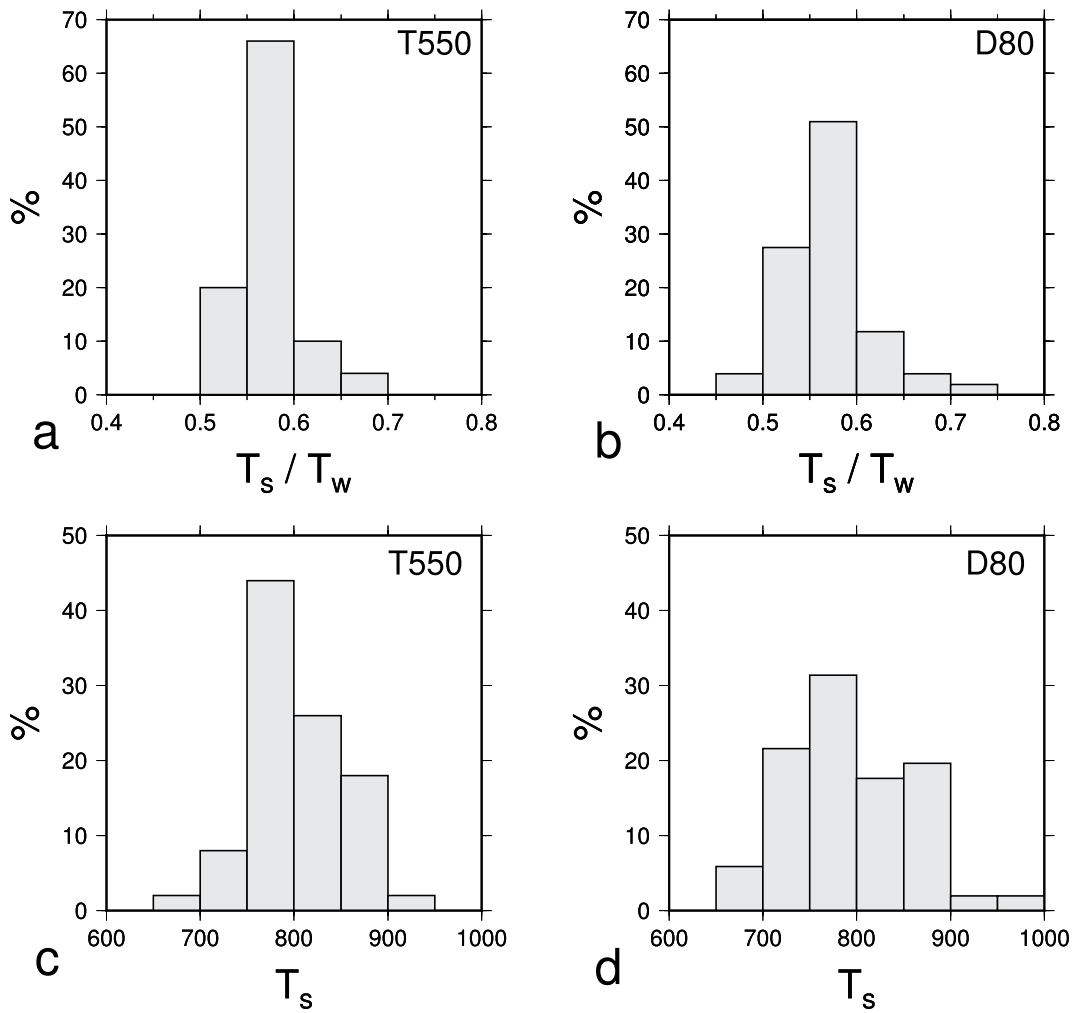

Figure 4. Relation between maximum temperature in the wedge and temperature at the top of the lower plate for calculations of Syracuse et al. (2010). (a) Ratio of temperature T_s at the top of the lower plate beneath the volcanic arc to T_w, maximum temperature in wedge above this point, when the top of the wedge-slab interface is constrained to be at a temperature of 500°C (Syracuse et al., 2010, Tables 2 and 3 [T550]). (b) As for (a), except for the calculations in which the base of the transition was constrained to be at 80 km (Syracuse et al., 2010, Table 3 [D80]). (c and d) Distributions of T_s from the calculations illustrated in (a and b).

The balance between diffusion and advection near the wedge-slab interface (Equations 7–10) explains the slow variation of temperature with depth, and relates temperature on the interface to maximum temperatures in the wedge (e.g., Figure 4). In analyzing temperatures from HPLT terrains that may have experienced conditions on the wedge-slab interface (Section 4.2), we shall rely on these simple and robust features of that interface.

4. Are HPLT Terrains Representative of Present-Day Subduction Zones?

Early discussions of high-pressure-low-temperature metamorphism concluded that the P-T data are consistent with conditions in present-day subduction zones (e.g., Ernst, 1971, 1973, 1975; Miyashiro, 1972, 1973; Oxburgh & Turcotte, 1971; Peacock, 1992). Some recent studies have, however, argued that data from HPLT terrains represent special conditions of preservation that are not relevant to subduction zones in general and, specifically, that HPLT rocks record temperatures that are hundreds of °C higher than found by numerical modelers (e.g., Abers et al., 2017; van Keken et al., 2018). Others have argued that shear heating on the plate interface explains the observed temperatures (e.g., Kohn et al., 2018; Penniston-Dorland et al., 2015). Under the latter interpretation, these rocks contain information on processes occurring at otherwise inaccessible depths on present-day subduction interfaces; under the former, they do not. We now analyze this issue using the framework established in Section 3.

Figure 1a shows a change in the trend of P-T data at around 1.5 GPa, with data below this pressure following a slope of ∼11 ± 3°C/km (Figure 1c), and those above showing weak, if any, dependence on pressure and being in the range of 560 ± 80°C (Figure 1b). The dependence of temperature on depth in the first of these groups is characteristic of plate interfaces (Section 3.2.1) and its near-independence of depth is characteristic of wedge-slab interfaces (Section 3.2.2.) In practice, because of the variation in maximum depth of thrust faulting (Figure 1a), we should expect that some points at ∼550°C and pressures lower than 1.5 GPa came from shallow wedge-slab interfaces, while some at pressures higher than 1.5 GPa came from deep plate interfaces. We therefore discuss the trends shown by the ensemble of data, which are more informative than individual data points.

4.1. P-T Data Shallower Than 1.5 GPa, Probably Relevant to the Plate Interface

If shear stresses on plate interfaces are assumed to be negligible, then Equation 1 may be rewritten, with $\tau' = 0$ as

$$\frac{T_f}{z_f} = \frac{Q}{K S_Q}. \tag{11}$$

Figure 5 shows the temperature gradients that would be maintained along the plate interface in the absence of shear heating, as a function of S_Q and age of the ocean floor. The lower-right and upper-left panels of Figure 5 show the distributions of age of the ocean floor and S_Q in 82 profiles across present-day subduction interfaces investigated by England (2018); here, S_Q is evaluated at the observed maximum depth of thrust-faulting earthquakes. At those depths, S_Q lies in the range $4 \le S_Q \le 13$, and in 90% of the cases the ocean floor is older than 25 Myr. The gray box delineating those ranges of S_Q and age in Figure 5 shows that, in the absence of dissipative heating, those segments could maintain temperature gradients no higher than 8°C/km, and for most of the range, 4°C/km or less. For the range of S_Q in present-day subduction zones, the age of the ocean floor would have to be $\lesssim$12 Myr ($S_Q = 4$) to $\lesssim$4 Myr ($S_Q = 14$) in order to maintain gradients equivalent to those recorded by HPLT rocks (11 ± 3°C/km, Figure 1). This analysis, in considering the full relevant range of parameter space, reinforces the conclusions based on a range of numerical calculations (e.g., Abers et al., 2017; van Keken et al., 2018) that, if shear heating on the plate interfaces were negligible, then the conditions recorded by HPLT rocks would not be representative of present-day subduction zones.

If, however, it is allowed that dissipation could have been occurring on plate interfaces while the HPLT rocks formed, then Equations 1–5 may be used to estimate the level of shear stress required to explain the P-T data. Rearranging Equation 1

$$\tau' = \frac{S_\tau}{V}\left(K T_f / z_f - Q / S_Q\right) \tag{12}$$

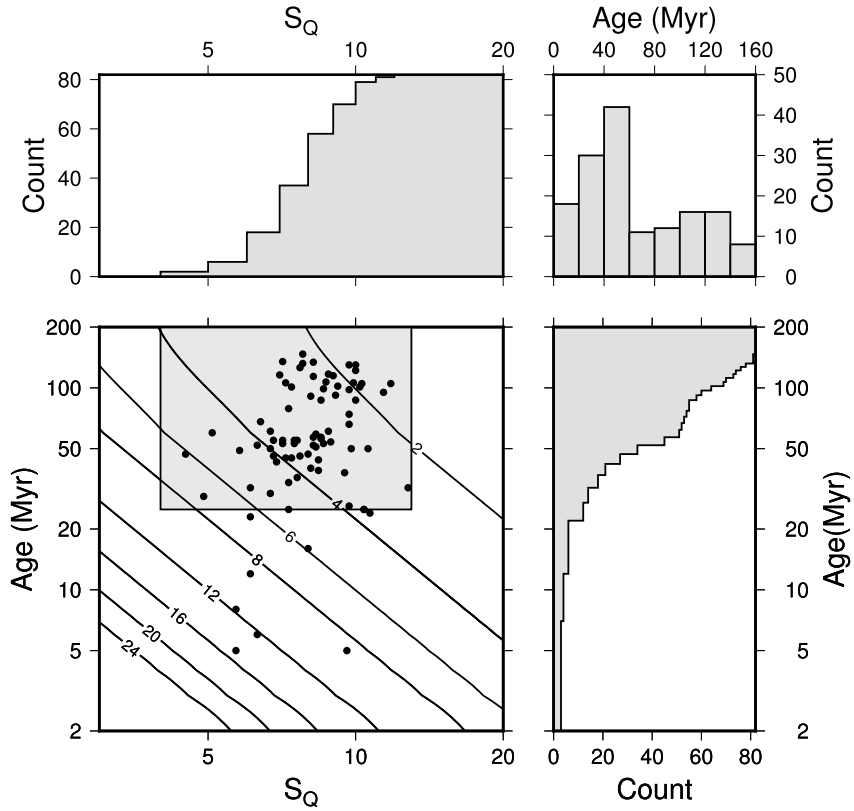

Figure 5. Temperature gradient along a plate interface in which there is no dissipative heating. The interface has a parabolic form, characteristic of present-day plate interfaces, with depth z_f depending on horizontal distance x from the trench as $z_f = cx^2$; here $c = 1.5 \times 10^{-3}$ km^{-1}, which is the median of c calculated for present-day plate interfaces (England & May, 2021). Solid lines in the main panel show dependence of temperature gradient (T_f/z_f, Equation 11) on S_Q (Equation 2) and age of ocean floor (with heat flux, Q, calculated from Parsons and Sclater [1977]). Cumulative histogram in upper-left panel shows the distribution of S_Q, calculated at the maximum depth of thrust-faulting earthquakes on the plate interface, for 82 profiles across present-day subduction zones (England, 2018). Dots in main panel show (S_Q, Age) for the 82 profiles. Upper-right and lower-right histograms shows distribution of ages of ocean floor for the profiles across subduction zones of SubMap 4.3 (Heuret et al., 2017); the 154 profiles used exclude those for which convergence velocities are uncertain (principally those involving small plates in the south-west Pacific), or for which the age of ocean floor is unavailable. Gray shading is bounded by an age of 25 Ma for the ocean floor and by the range of S_Q for present-day subduction zones.

$$\mu' = \frac{S_\tau}{V g \rho z_f} \left(K T_f / z_f - Q / S_Q \right). \tag{13}$$

Figure 6 shows the ranges of effective coefficient of friction, μ', and effective stress, τ' that would be required if dissipative heating were to maintain a temperature gradient of $T_f/z_f = 11$°C/km on the plate interface, with lower plate of age 55 Myr (the median age of the profiles: top-right panel of Figure 5). The upper-left panel of Figure 6 shows the distribution of V for the 154 present-day subduction segments of SubMap 4.3 (see Figure 5); 131 of those segments have $50 \leq V \leq 125$ mm/yr. The lower-right panel shows the distribution of distance along the interface, u_T, between the trench and the maximum depth of thrust faulting on the interfaces for the 82 profiles of England (2018); 73 of the interfaces have $100 < u_T < 300$ km. The gray box delineating those conditions in Figure 6 shows that the effective coefficient of friction on the plate interface is required to be $\mu' \sim 0.065$–0.075 (solid contours in Figure 6). If it is assumed that the shear stress during slip is independent of depth, then those stresses lie between 25 MPa and about 125 MPa (dashed contours in Figure 6).

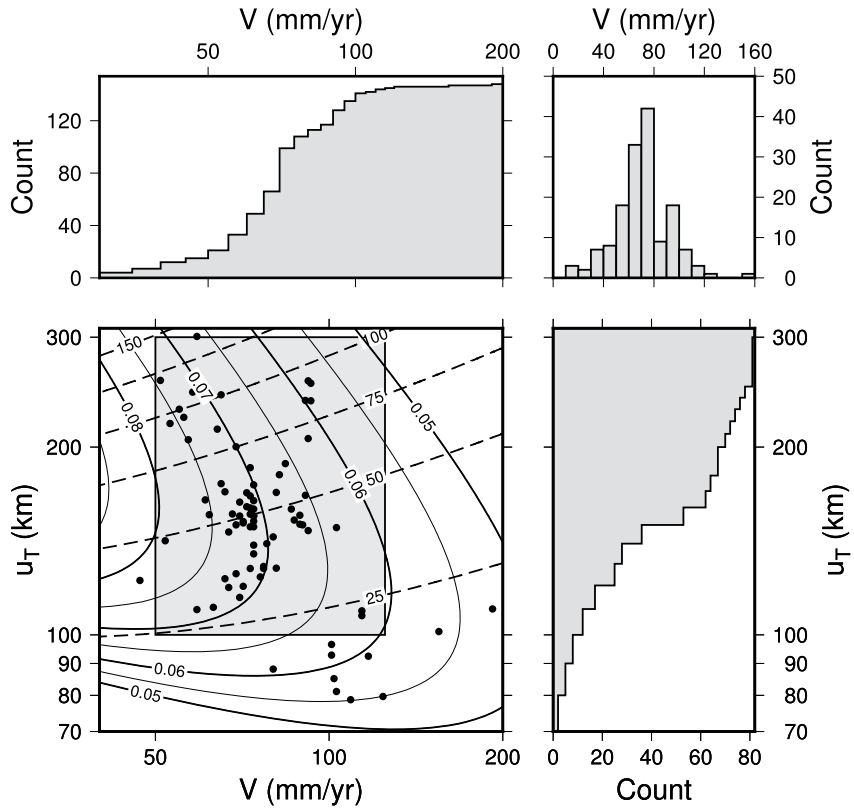

Figure 6. Values of shear stress during slip required to maintain a temperature gradient of 11°C/km along a plate interface by heat from the lower plate plus dissipative heating. Interface shape as in Figure 5. Solid lines are contours of μ' calculated from Equation 13 with $Q_0 = 0.064$ mW/m^2 (equivalent to ocean floor of age 55 Myr). Dashed lines are calculated from Equation 12. Cumulative histogram in the lower-right panel shows the distribution of distance along the interface from the trench to the maximum depth of thrust faulting, u_T, for the 82 profiles of England (2018) across present-day subduction zones. The upper histograms show distribution of velocities, V, for the 154 profiles of SubMap 4.3 (see Figure 5). Dots in the main panel show (V, u_T) points for those profiles; see text for the boundaries to the gray shading.

This analysis demonstrates that, for the ranges of convergence speed and plate boundary length pertinent to present-day subduction zones, the P-T data can be fit with geophysically reasonable shear stresses—as has been suggested, for example, by Kohn et al. (2018), Peacock (1992), and Penniston-Dorland et al. (2015). The required shear stresses during slip are consistent with independent estimates of shear stress on the interface from measurements of heat flux (Table 2). Figure 7 shows that the temperature rises due to the dissipative heating amount to several hundreds of degrees (see also Penniston-Dorland et al. [2015], Figure 9).

Figure 8 compares the P-T data with temperatures on the plate interface calculated from Equation 1 for the subduction segments of Table 2, using the appropriate values of convergence rate, dip, and Q_0 for each interface, with μ' as determined from the heat flux observations by England (2018). The profiles are calculated from the surface to the maximum depth of thrust-faulting earthquakes for each segment, which varies from about 20 km on the Hikurangi margin (Profile [1], Figure 8, temperature ~250°C) to over 60 km beneath Kamchatka (Profile [9], temperature ~650°C). The calculated thermal profiles span the range of P-T conditions observed in HPLT terrains (Figure 1).

We emphasize, as will be discussed more fully in Section 5.1 that, for most plate interfaces, the conversion of mechanical energy into heat takes place primarily in earthquakes, with the effective coefficient of friction, μ', representing dynamic stresses during the rupture process (e.g., Kanamori & Rivera, 2006). It is noteworthy, in this context, that the few reports of pseudotachylites from subduction settings are from rocks whose ambient P-T conditions lie within the field of the HPLT data we analyze here (Figure 8). They lie toward the high-temperature end of the field, as would be expected because temperatures are lower both above and below the source of heat—see Figure 12a.

Table 2
Estimates of Effective Coefficient of Friction, μ', From Profiles of Surface Heat Flux Above Plate Interfaces (England, 2018; Gao & Wang, 2014)

Profile	Gao and Wang (2014)		England (2018)		z_T[a] (km)	$\tau\,(z_T)$[b] (MPa)
	μ'[c]	μ'[d]	μ'[e]	μ'[f]		
N. Hikurangi	0.13		0.07	0.02–0.12	35	75
British Columbia	0–0.06	0.02	0.07[g]	0–0.14[g]	40	85
Nankai	≤0.03	0.03	0.05	0.04–0.08	35	65
Manila		0.09	0.06	0.02–0.11	40	73
N. Honshu		0.025	0.05	0.03–0.08	52	80
N. Sumatra	<0.08	0.03	0.06	0.02–0.09	55	100
N. Kermadec	~0.07		0.05	0.04–0.06	52	80
S. Kermadec			0.05	0.03–0.07	52	80
Kamchatka	<0.09	0.03	0.05	0.02–0.07	61	95

Note. The reader is referred to the Supplementary Materials of Gao and Wang (2014) and to Section 2.3 and Appendix B of England (2018) for discussion of uncertainties associated with these estimates, and for review of other estimates of, and assumptions about, shear stresses on those plate boundaries. The profile of Gao and Wang (2014) for southern Chile is omitted because the maximum depth of the slab beneath the heat flux measurements is 10 km, less than the pressure range that we consider.

[a]Maximum depth of thrust faulting, z_T, from England (2018, Figures 2–4 and B1–B5). [b]Shear stress at z_T, calculated using an average density of 3,100 kg m^{-3} for the upper plate. [c]Gao and Wang (2014) best, or range of, fit. [d]Gao and Wang (2014) preferred value. [e]England (2018) best fit. [f]England (2018) range. [g]See (England, 2018, Section 3.1.3, and Figure 4) for discussion of uncertainties in the influence of hydrothermal cooling of young oceanic lithosphere that yield a large range in acceptable values of μ', with no clear best fit. The value used here is in the middle of that range.

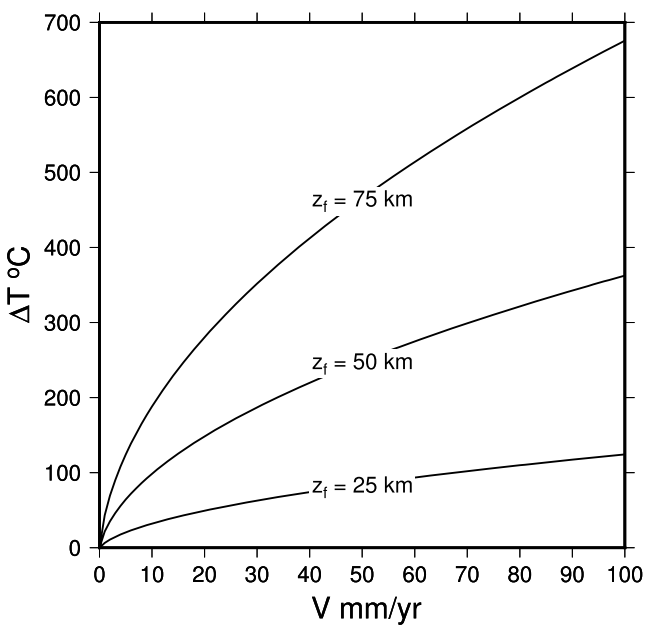

Figure 7. Illustration of temperature increases, ΔT, arising on the plate interface due to dissipative heating. Curves, labeled with interface depth, show the dependence on convergence rate of temperature increases calculated from the second term on the right-hand side of Equation 1. For this illustration, the plate interface is taken to be planar, with sin(dip) = $\frac{1}{4}$. Temperature rises are proportional to μ', which is taken here to be 0.06. The average density of the upper plate is taken to be 3.1 Mg m^{-3}and the remaining parameters are given in Table 1.

4.2. P-T Data Deeper Than 1.5 GPa, Probably Relevant to the Wedge-Slab Interface

The P-T data at pressures greater than 1.5 GPa show weak, if any, dependence on pressure and lie in the range of 560 ± 80°C (Figures 1a and 1b). In the light of Section 3.2, which showed that temperatures in the wedge-slab interface are—relative to those in the plate interface—insensitive to pressure, it is reasonable to treat the ensemble of these data as representing conditions in the wedge-slab interface. The steep decrease in temperature with depth beneath the top of the interface (Equation 6 and Section 3.2.2) results in considerable variation of temperature at constant pressure within the interface, and we expect that only the highest among these temperatures represent conditions near the top of the interface. With a small number of exceptions, temperatures in this set of data do not exceed 650°C (Figures 1a and 1b). The scaling arguments of Section 3.2.2 and Figures 4a and 4b then suggest that the maximum temperature in the wedge above those interfaces would have been ~(650/0.6 ≈ 1100)°C. These temperatures do not approach the temperatures of 700–900°C that are calculated for the slab top beneath the arc volcanoes (e.g., England & Katz, 2010; Syracuse et al., 2010, Table 3, and see Figures 4c and 4d above).

4.3. Summary

Although measured temperatures from pressures ≲1.5 GPa in HPLT terrains are higher than the outputs of some numerical models (e.g., van Keken et al., 2018), they are entirely consistent with temperatures calculated for plate interfaces with dissipative heating at rates constrained by measurements of heat flux (e.g., England, 2018; Kohn et al., 2018; Molnar & England, 1990;

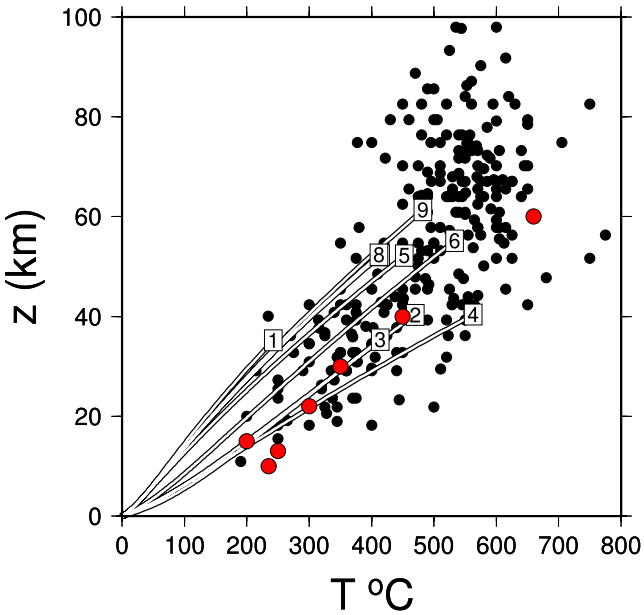

Figure 8. Comparison between P-T data from HPLT terrains and calculated conditions in present-day subduction zones. Black dots show the P-T data of Figure 1, with their uncertainties suppressed for clarity. Open lines show calculated temperature profiles along the top of the descending plate in subduction zones where shear stresses are constrained by surface heat flux measurements (England, 2018, see Table 2). Labels denote profiles as follow: (1) Hikurangi margin; (2) British Columbia; (3) Nankai; (4) Manila; (5) N. Honshu; (6) N. Sumatra; (7) N Kermadec; (8) which overlies (7) S. Kermadec; (9) Kamchatka; (for detailed locations see England, 2018). Red circles show ambient P-T conditions for rocks from subduction settings in which pseudotachylytes have been reported (Andersen et al., 2014; Ikesawa et al., 2003; John & Schenk, 2006; Magott et al., 2016; Menant et al., 2018; Okamoto et al., 2007; Pittarello et al., 2022; Rowe et al., 2011; Vitale et al., 2019).

Peacock, 1992; Penniston-Dorland et al., 2015, and see Table 2). Temperatures at pressures likely to be representative of the wedge-slab interface ($\gtrsim$1.5 GPa) are at least 100°C cooler than found in model calculations of temperatures for comparable locations; we return to this issue in Section 5.6.

5. Mechanics of Generation and Preservation of HPLT Terrains

Most of the ocean-floor sediment entering convergent plate boundaries is subducted with the rest of the oceanic plate (e.g., Clift & Vannucchi, 2004; Scholl & von Huene, 2007; von Huene and Scholl, 1991). This observation raises two questions. The first is: what mechanical conditions are required in order to subduct sedimentary sections whose average thickness is of order a kilometer (e.g., Scholl & von Huene, 2007)? The second is: given that protoliths for HPLT terrains are continually delivered to depth in present-day subduction zones, why are such terrains so rare in the geological record? Clearly, if rocks of the interface are denser than their surrounding plates or mantle wedge, there is no difficulty in subducting them, nor in explaining their absence from the record. This section analyses the subduction of material, such as sediment or hydrothermally altered mafic and ultramafic rock, that is less dense than the rocks either side of the interface.

In Section 5.1 we discuss the role of earthquakes and related phenomena in the burial of HPLT terrains. To address the remaining aspects of the questions above, we need expressions for flow in a dipping layer of buoyant power-law fluid, representing the interface rocks, which are derived in Appendix C and summarized in Section 5.2. These are used to analyze the capacity the subduction interface, in Section 5.3, the transition from descent to ascent within the interface (Section 5.4), and the ascent of rocks with the interface (Section 5.5) and from the wedge-slab interface (Section 5.6).

A note on terminology: Several terms commonly found in discussions of the mechanics of HPLT terrains have unclear or disputed meanings, and some carry imprecise mechanical connotations. Such terms include "coupling," which is defined in a number of ways, some of which contradict one another (see e.g., Wang & Dixon, 2004) and in some papers the term is not defined at all. Similar problems arise with the use of "accretion," "detachment," and "décollement" (e.g., Agard et al., 2018, Table 1). We avoid such terms, as far as we can. We shall refer to displacements and velocities in a frame of reference fixed to the upper plate.

5.1. Role of Earthquakes and Related Phenomena

In most present-day subduction zones relative motion across plate interfaces takes place predominantly in earthquakes and related phenomena, which include slip that, although slow in the seismological sense (days to years) (e.g., Beroza & Ide, 2009; Schwartz & Rokosky, 2007), is geologically rapid. The mean fraction of relative plate motion that is accommodated seismically in the present-day subduction zones examined by Scholz and Campos (2012) is between 60% and 70%. The instrumental record is probably too short to characterize accurately the long-term seismic moment release at plate interfaces (e.g., McCaffrey, 2008; Rong et al., 2014; Stein & Okal, 2007), so the contribution of earthquakes to long-term slip on apparently aseismic interfaces may be underestimated. It therefore seems probable that the downward displacement of material within most plate interfaces takes place primarily not by viscous creep, but during thrust-faulting earthquakes.

Most of the seismic relative motion across plate interfaces takes place in the few largest earthquakes (Brune, 1968; Molnar, 1979), which typically are great earthquakes ($M_w \gtrsim 8$), with tens of meters of slip over areas that are several hundred kilometers along-strike, and one or two hundred kilometers in the down-dip direction; most of the moment release in those earthquakes is in the depth range 20–50 km (Bilek & Lay, 2018). In addition, slow

slip events suggest that relative plate motion continues to be accommodated discontinuously deeper than the maximum depth of thrust faulting (see Section 3.1).

Although reports of pseudotachylites from HPLT terrains are scarce (e.g., Sibson & Toy, 2006), this does not imply that HPLT terrains were untouched by earthquakes. Even for great earthquakes, the shear planes are likely to be millimetric to centimetric in width and difficult to detect (e.g., Cowan, 1999; Rice, 2006; Rowe & Griffith, 2015; Sibson, 2003). Furthermore at temperatures of several hundred degrees (Figure 1), pseudotachylytes and other features associated with rapid slip may be erased swiftly (e.g., Fondriest et al., 2020; Kirkpatrick & Rowe, 2013; Kirkpatrick et al., 2009). In the companion paper (Smye & England, 2022) we discuss which of the lithologies present in the plate interface are likely to strain slowly enough under ambient conditions that the relative motion across the interface would likely be seismic.

5.1.1. Deformation During Seismic Descent in Plate Interface

The widespread observation that coseismic deformation in major earthquakes at subduction zones is reversed inter-seismically suggests that ductile deformation within the plate interface is generally small in comparison with overall rates of convergence which for, 90% of present-day subduction zones, lie in the range 30–100 mm/yr (Heuret et al., 2017; Jarrard, 1986, and see Figure 6). If 10% of those rates were absorbed aseismically, the equivalent strain rates would be in the range 3×10^{-14} to 3×10^{-11} s^{-1} for interface thicknesses between 3 km and 100 m.

If HPLT terrains were subducted the same fashion as present-day ocean-floor rocks, then the ductile deformation they record would represent only a small fraction of their down-dip displacement, most of which was seismic. That ductile strain may, nevertheless, be significant: to reach the conditions recorded in Figure 1, rocks must have traveled along their interfaces for between 100 and 300 km (Figure 6); if 10% of that relative motion were absorbed across a 100 m-to-3-km interface, the average finite shear strain would be between ∼300 and ∼3.

Displacements of 100–300 km across the interface are equivalent to slip in $\sim 10^4$ great ($M_w > 8$) earthquakes. During that motion, the interface will also have experienced $\sim 10^5$ $M_w > 7$ earthquakes, each of which involved slips of a few meters on fault planes having areas of several times 10^4 km^2. It seems probable that, during the time over which those tens of thousands of earthquakes took place, the principal plane(s) of shear would migrate within the interface. Were they to migrate downwards within the interface, they would generate relations that are often referred to as "accretion" (e.g., Agard et al., 2018, Table 1) or "underplating" (e.g., Shreve & Cloos, 1986). If a shear plane were to migrate downwards from sediments into mafic portions of the upper crust of the lower plate, then the resultant stratigraphic relationship would resemble what is often referred to as "detachment" (e.g., Agard et al., 2018, Table 1).

Accretion and detachment are sometimes argued, on the basis of field observations, to require special tectonic conditions (e.g., Agard et al., 2018; Bialas et al., 2011); a more parsimonious interpretation is that migration of major slip planes is a commonplace result of accommodation of hundreds of kilometers of convergence across plate interfaces by slip in large-to-great earthquakes. The implications of this process for PTt paths are discussed in Section 6.

5.2. Flow of the Interface

We now consider ductile deformation of the subduction interface, which probably applies to aseismic plate interfaces, and to wedge-slab interfaces. The physical properties of the interface are governed by a large number of parameters that are poorly constrained by observation; these include temperature, pressure, pore-fluid pressure, and intrinsic physical properties of the widely differing rock types that make up the interface (e.g., Fagereng & Sibson, 2010; Fagereng & Toy, 2011). Deformation within the interface has been examined with rheological models that range from a single Newtonian fluid (e.g., England & Holland, 1979; Shreve & Cloos, 1986) to multiple lithological units, each with its own rheological parameters (e.g., Gerya et al., 2002; Z. H. Li et al., 2011). The main questions may, however, be addressed by a general analysis that does not depend on details of the rheological properties of rocks in the interface.

We employ a power-law relationship between shear stress, τ, on the interface and velocity gradients within it,

$$\tau = C \frac{\mathrm{d}v}{\mathrm{d}y} \left| \frac{\mathrm{d}v}{\mathrm{d}y} \right|^{1/n-1}. \quad (14)$$

Here C contains the dependence of strain rate on temperature (Equations C1–C6). An equivalent form holds for aggregates of minerals (Huet et al., 2014), so Equation 14 is appropriate for a wide range of cases.

We treat the interface as having thickness h; the x-coordinate is in the down-dip direction; the base of the layer is at $y = 0$, and y increases upwards. If the layer is thin in comparison with its depth, and h changes slowly in the down-dip direction ($\mathrm{d}h/\mathrm{d}x \ll 1$) then, neglecting accelerations, the stress balance may be written as

$$\frac{\mathrm{d}\tau}{\mathrm{d}y} = C\frac{\mathrm{d}}{\mathrm{d}y}\left[\frac{\mathrm{d}v}{\mathrm{d}y}\left|\frac{\mathrm{d}v}{\mathrm{d}y}\right|^{(1/n-1)}\right] = g\sin(\delta)\Delta\rho = \Phi, \tag{15}$$

$$\tau(h) = \tau(0) + \Phi h \tag{16}$$

(e.g., Batchelor, 1967, pp. 182–183 and 220, and England & Holland, 1979; Shreve & Cloos, 1986). Here τ is the shear stress acting on planes parallel to the layer, with negative τ corresponding to x-velocity decreasing upwards; g is the acceleration due to gravity, δ is the dip of the layer, and $\Delta\rho$ is the average density of the overburden minus the density of the layer. We shall refer to Φh as the buoyancy stress.

We first consider the case in which all material within the interface moves down-dip, in the x-direction, which requires $\tau(h) \leq 0$. This condition is met when the shear stress at the base, $\tau(0)$, $\leq -\Phi h$ (Equation 16). For a typical dip of 20° of the plate interface, a density contrast between upper plate and interface material of ∼500 kg m^{-3} and for interfaces of width ∼1–3 km, the buoyancy stress is ∼1–5 MPa (see also England & Holland, 1979; Shreve & Cloos, 1986).

In Appendix C1 we obtain an expression for the velocity in terms of the power-law exponent, n, and the quantity γ, which is the negative of the shear stress on the top of the interface divided by the buoyancy stress Φh (Equation C13)

$$v = V\left(\frac{(1+\gamma-y/h)^{n+1} - \gamma^{n+1}}{(1+\gamma)^{n+1} - \gamma^{n+1}}\right), \tag{17}$$

(Equation C15 and C16).

When γ is small, flow is concentrated toward the base of the interface, the more so the greater is n (Figure 9a). As γ increases, the velocity tends toward a linear gradient between top and bottom of the interface

$$\lim_{\gamma\to\infty} v = V\left(1 - \frac{y}{h}\right). \tag{18}$$

Even when $\gamma = 3$ (Figure 9b), the gradient is close to linear and for $\gamma \gtrsim 10$ departures from linearity are negligible (Figure 9c). As an example: for interface thickness of 2 km, the buoyancy stress is of order 3 MPa, so velocity gradients across the interface are close to linear once the shear stress on the interface exceeds about 10 MPa.

After the cessation of subduction, $v(0) = v(h) = 0$. In this case

$$v = -\frac{h}{2(n+1)}\left(\frac{\Phi h}{2C}\right)^n\left(1 - \left|\frac{y}{h}\right|^{n+1}\right), \tag{19}$$

where $y = 0$ is now in the center of the layer $-h/2 \leq y \leq h/2$ (Appendix C2). This generalizes the solution of Turcotte and Schubert (2014, p. 357), allowing n to have any real positive value.

Appendix C4 considers the influence of temperature dependence on the fluid flow, which is governed by two dimensionless parameters. One relates the activation energy, E, to the characteristic absolute temperature, Θ, of the interface and to the temperature difference $\Delta\Theta$ across it,

$$E' = \mathrm{Br}\frac{E\Delta\Theta}{R\Theta^2}, \tag{20}$$

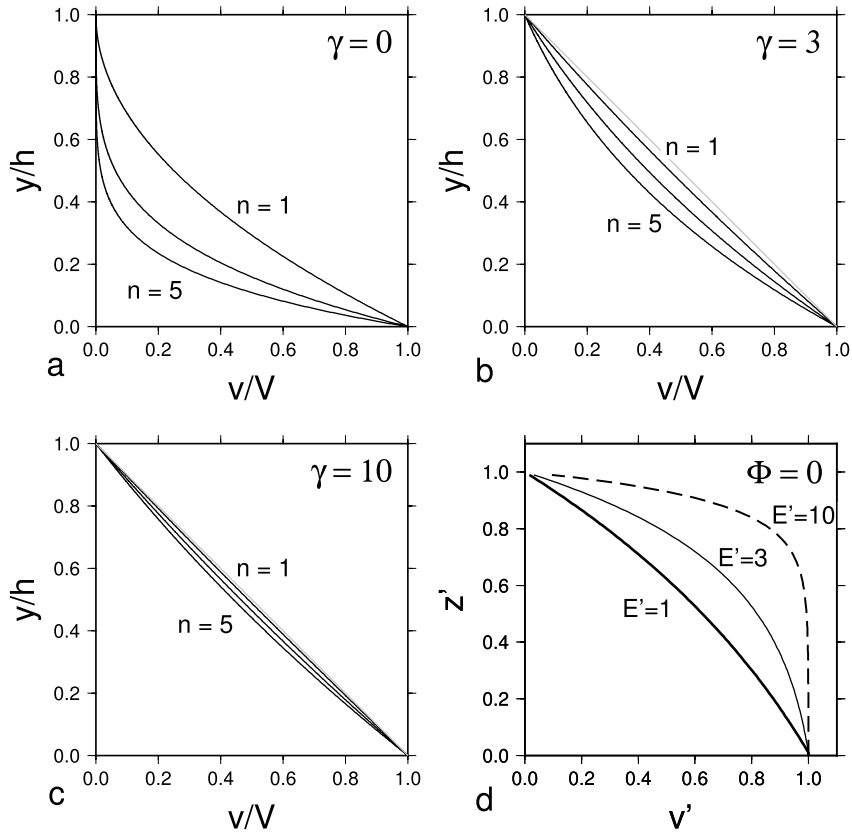

Figure 9. Dependence of profiles of descent speed on γ (Equation 17) and E' (Equations 20 and C39). (a–c) Evaluation of Equation 17 for power laws of 1, 3, and 5, and for $\gamma = 0$, 3, and 10. (d) Profiles of downward velocity for a Newtonian fluid with temperature-dependent viscosity (Equation C39), with $\boldsymbol{\Psi} = 0$, equivalent to $\gamma \to \infty$. Thick, thin, and dashed lines show profiles for, respectively, $E' = 1$, 3, and 10.

(Equation C37). Here Br is the Brinkman number, which is the ratio of viscous dissipation, τV, to the conductive flux of heat across the interface, $K\Delta\theta/h$, and is of order one for the cases we consider (Appendix C4). For common rock-forming minerals, E is between 1 and 5×10^5 J mol^{-1} so, with $\Theta \sim 1000$ K, and $\Delta\Theta \sim 100$ K, E' lies in the range ~1–10. The second parameter (Equation C38) is

$$\Psi \sim \frac{\Phi h}{\tau}. \tag{21}$$

For descent along many plate interfaces, Ψ is small, as discussed above, so we illustrate the influence of temperature-dependent rheology on velocity profiles during descent using Equation C39 with $\boldsymbol{\Psi} = 0$ (Figure 9d). The influence of temperature differences on the velocity profile across the interface is modest unless $E' \gtrsim 3$, when shear becomes concentrated in the top $1/E'$ of the interface, and the rest of the interface descends at the velocity of the lower plate.

After subduction ceases there is no velocity difference between top and bottom of the interface, and velocities within the interface are proportional to Ψ (Equation C39). Again the influence of temperature gradients on the velocity profile is small for $E' \lesssim 3$ (Figure 10a). Because the thermal gradient due to dissipative heating drops quickly after cessation of subduction (Figure 12), it is probable that $E' \lesssim 1$ and that the influence on return flow of temperature variation across the interface is less significant than that of lithological variation.

5.3. Capacity of the Subduction Interface

The local capacity of the interface (Shreve & Cloos, 1986) is the maximum flux of material that can be sustained at the point of interest, for given convergence rate and properties of the interface. Shreve and Cloos (1986) provide an illuminating discussion of the response of the interface to changes in sediment supply, which we

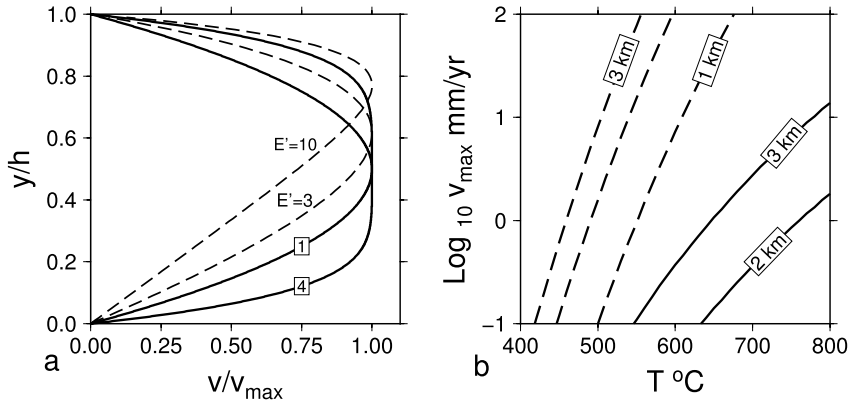

Figure 10. Ascent speeds in the subduction interface. (a) Solid lines show profiles of upward velocity for fluids with power-law rheology with $n = 1, 4$ (Equation C1 and C20). Dashed lines show profiles of upward velocity for a Newtonian fluid with temperature-dependent viscosity with $E' = 3$ and 10 (Equation 20 and C39). (b) Rates of ascent of sheets of interface, of thickness 1, 2, and 3 km and density contrast 500 kg m^{-3} with overburden. Rates are calculated from Equation 19 with the rheological parameters for aragonite given by Rybacki et al. (2003) (dashed lines) and wet quartzite Hirth et al. (2001) (solid lines).

discuss briefly in Section 6.2. Here, we confine our attention to the specific issue of the local capacity of the interface, which determines the thickness of buoyant material that may be subducted to any depth of interest. Buoyant material may rise from the wedge-slab interface (e.g., Behn et al., 2011; Gerya & Stöckhert, 2006; Miller & Behn, 2012), so the concept of interface capacity is relevant principally to the plate interface.

If the interface behaves as fluid, with temperature independent of y, it is at its capacity when $\gamma = 0$, equivalently when the shear stress on its base is equal to the buoyancy stress, Φh. Equation C26 shows that the local capacity is approximately proportional to convergence rate, V (for $n \gtrsim 3$, as is commonly the case for rock-forming minerals), and declines strongly as its temperature increases. We illustrate the principal features of this behavior by evaluating the expression for capacity (Equation C26) using the rheological parameters of wet quartzite and aragonite. We emphasize that these calculations are purely illustrative, they are uncertain by at least a factor of ten—and far greater than that if the influence of dissolution-precipitation creep is considered (Smye & England, 2022, Section 4 and Figure 13). Figure 11 shows that interface capacity of rocks having the rheological properties of wet quartzite (Hirth et al., 2001) drop from ~10 km at 300°C to of order 1 km at 800°C. The equivalent thicknesses for an interface with the properties of aragonite (which probably is stronger than most other carbonate minerals, Rybacki et al., 2003) range between 10s of km and ~100 m.

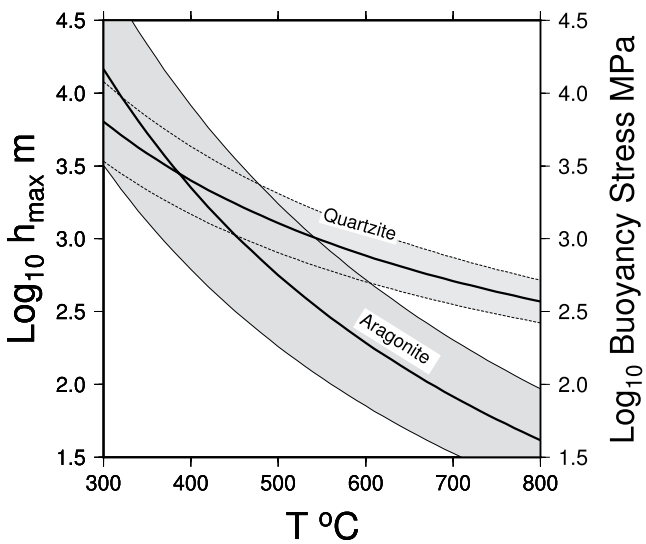

Figure 11. Local capacity of plate interface for specimen rock types. Capacities are expressed as effective thickness, h_{local} (Equation C26), for interfaces with the rheological parameters of wet quartzite and aragonite; gray bands show ranges of capacity associated with uncertainties in activation energy (Table 3). Buoyancy stress (right-hand axis) is the product of h_{local} with g, a density contrast of 500 kg m^{-3} and a dip of 20°.

5.4. Transition From Descent to Ascent

The previous section argues that shear stresses in active subduction interfaces are generally much greater than buoyancy stresses, implying that a significant departure from the prevailing force balance is required if the rocks within an interface are to return to shallow depths. The ratio of exhumed HPLT material to subducted oceanic crust is small ($\lesssim$2%, e.g., Agard et al., 2009), which further implies that exhumation is inefficient in comparison with subduction. The purpose of this section is to focus on processes that are clearly linked to the required change in force balance, and to determine how, or whether, observations of HPLT rocks may be used to discriminate among them.

5.4.1. Cessation of Subduction

The simplest explanation for the exhumation of interface material is the cessation, or slowing by a large fraction, of the convergence across the interface (e.g., England & Holland, 1979; Ernst, 1970, 1975, 1988; Platt, 1993). Modern plate interfaces appear to support shear stresses much greater than the buoyancy

Table 3
Rheological Parameters Used in Figure 11 and Viscosities for a Shear Stress of 3 MPa at Different Temperatures and a Pressure of 2 GPa

Mineral	A (MPa^{-n} s^{-1})	E (kJ/mol)	n	Viscosity Pa s		
				400°C	550°C	700°C
Quartzite[a]	6.3×10^{-12}	135 ± 15	4	2×10^{21}	2×10^{19}	1×10^{18}
Aragonite[b]	200	240 ± 29	3	5×10^{20}	2×10^{17}	9×10^{14}

[a]Hirth et al. (2001). [b]After Rybacki et al. (2003), see discussion in Section 4.1 of Smye and England (2022).

stress, regardless of convergence rate (e.g., Table 2), so the transition from subduction to exhumation requires a major reduction in shear stress on the interface. With laboratory experiments yielding values of ~3 to 5 for the power-law relation between strain rate and stress for many minerals, reduction in shear stress by a factor of two would require convergence rates to drop by a factor of 8–32; correspondingly greater reductions in rates would be required for greater reductions in stress. Such reduction may occur either in response to changes in large-scale plate motions or because convergence shifts to a new interface. In either case, because downward tractions are greatly reduced or removed, rocks are free to move back up the interface. Major reorganizations of subduction zones are rare, so this requirement helps to explain the rarity of HPLT terrains (e.g., Monié & Agard, 2009). Recent high-resolution reconstructions using marine magnetic anomalies show rapid (few Myr) changes in plate motion (e.g., Croon et al., 2008; DeMets & Merkouriev, 2019, 2021; Demets et al., 2015), some of which may linked to rearrangement of subduction boundaries.

The ascent of a package of rocks along the interface results in normal-sense shear at the top of the package and reverse-sense shear at its base; such a flow can also entrain much denser blocks if they are small with respect to the interface thickness and/or the material of the interface has a yield stress of a few Pa (e.g., England & Holland, 1979). Although this process has been called "diapiric ascent" by Maruyama et al. (1996), the rocks remain confined to the interface and do not penetrate their overburden.

It may be necessary to repeat that attribution of exhumation to thrusting is erroneous (England & Molnar, 1990). Although this point was clearly made by Platt (1993) in a review of exhumation of HPLT terrains, the mechanism is still sometimes invoked (e.g., Guillot et al., 2009, p. 182, in discussion of their Figure 4).

5.4.2. Break-Off or Retreat of Slabs

A mechanism frequently proposed to explain exhumation of HPLT terrains is separation of part of the slab from the lower plate. Gaps in intermediate-depth seismicity suggest that this process does occur (e.g., Isacks et al., 1968; McCaffrey et al., 1985), and it has been suggested as the cause of surface uplift at the New Hebrides plate boundary (Chatelain et al., 1992). We are not aware, however, of a mechanical analysis that clearly demonstrates a link between breaking of slabs and ascent of HPLT terrains within the subduction interface. Indeed, it is not obvious that this process, alone, should lead to exhumation of HPLT rocks: the descent of material in the interface is driven by the shear tractions within the interface, not by the negative buoyancy of the slab below. If the loss of negative buoyancy of the slab leads to cessation of subduction, then the mechanical considerations are those of Section 5.4.1. If, however, convergence continues at a rate imposed by large-scale plate motion, as is the case for example, in the New Hebrides (Chatelain et al., 1992), then the downward shear traction in the remaining parts of the subduction interface should not be substantially affected, and exhumation would not be expected.

In a review of slab break-off, Garzanti et al. (2018) describe how the process is invoked not only for the exhumation of the subduction interface but also to account for an immense range of geological phenomena in virtually every mountain belt on Earth, from Archean time to the present. The notion of slab rollback has, similarly, been invoked as a cause of exhumation of HPLT rocks, among many other phenomena. The principal mechanical influence of rollback is to make horizontal tractions on the plate interface slightly less compressional than lithostatic pressure (Le Pichon, 1982). Calculations of the attendant reductions in shear stress indicate that they are of the order of a few tens of percent (Husson et al., 2009), which are small in comparison with the many-fold reduction that is likely to be required if shear stresses are to become smaller than buoyancy stresses (Section 5.4.1).

It is worth considering the field relations that would be observed if either the breaking off or the rolling back of a slab were to lead to exhumation. The motion of rocks within the interface depends only on the local relative magnitudes of buoyancy and shear stresses, we should therefore expect the same field relations whether exhumation arises from cessation of subduction, the break-off or retreat of a slab, or indeed from any other process that leads to buoyant ascent of material within the interface. Attributing exhumation to any one of these processes, on the basis of observations that are consistent with all of them, is an unprofitable exercise.

Finally, we note that both rollback of, and breaks in, slabs are widespread at present, so an additional argument is required to make either of these a convincing cause for a phenomenon that is rare in the geological record. We

repeat the warning of Garzanti et al. (2018) that one should be alert to the conversion of hypothesis into factoid by amplification, distortion, or transmutation of citations (see Greenberg, 2009, for definition of those terms).

5.5. Ascent of Material Within the Subduction Interface Following Cessation of Subduction

When shear stress associated with relative motion of the bounding plates is removed, or greatly decreased, buoyancy stress dominates. Individual packages of rock within the interface will rise at different rates; in particular, packets of rock that are less dense, or have lower strengths, than rocks higher up the interface will move more rapidly up the interface, increasing the thickness—and hence the ascent speed—of rocks in the interface above. We show in Appendix C5 that, provided the effective viscosity of rocks in the interface is lower than about 10^{19} Pa s, this type of instability could develop within a million years of the cessation of subduction.

Ascent speeds of individual packages will depend heavily on their rheological parameters, on their thicknesses, and upon their temperatures. We discuss this process in more detail in the companion paper (Smye & England, 2022), once we have determined the properties of the interface for specific protoliths, but we can make some general remarks here. The ascent speed of a packet of rock described by a rheology with power-law exponent n is proportional to the $(n + 1)^{th}$ power of its thickness (Equation C20). Values of $n \sim 3$–4 are commonly determined from laboratory studies of minerals and rocks, thus thickening of the interface by a factor of two would increase ascent rates by factors of 16–32; tripling the thickness would induce up to hundred-fold increases in rates.

For fluids with a power-law exponent of 3 or more, speeds throughout most of the interface are close to the maximum value, giving a plug-like form to the flow (Figure 10a, Equation 19). Speeds depend strongly on temperature, and upon thickness, because of their power-law dependence on this quantity (Equation C20). We illustrate these factors in Figure 10b by showing ascent speeds for homogeneous interfaces of thickness 1, 2, and 3 km with the rheological parameters of aragonite (Rybacki et al., 2003) and wet quartzite (Hirth et al., 2001). In this illustrative example the ascent speed for the 3-km unit of aragonite drops from $\gtrsim$100 mm/yr at ~550°C to $\lesssim$0.1 mm/yr at ~420°C; the ascent speed of a 3-km-thick unit of quartzite drops from ~10 mm/yr at ~800°C to less than 0.1 mm/yr at ~550°C.

Figure 10b shows that, for a single homogeneous unit, more than a hundred-fold change in ascent speed can result from variation in its thickness by a factor of three, or in its temperature by ~100°C. Rates of ascent in real subduction interfaces are likely to be further influenced by contrasts in effective viscosity and shear zones associated with variation in lithology, strain history, pore fluid pressure, and metamorphic reactions. It is therefore clear that buoyant ascent of interface material following cessation of subduction is likely to result in complex and unpredictable juxtaposition and intercalation of tectonic units.

5.6. Diapiric Ascent From the Wedge-Slab Interface

Ascent of rocks of the plate interface is constrained, by the rigidity of the overlying plate, to lie within the interface. That constraint does not apply to rocks of the wedge-slab interface; indeed, whereas we have argued (Section 5.4) that ascent within the plate interface requires significant reduction, or cessation, of shear stresses associated with plate relative motion, rocks of the wedge-slab interface may rise continually into the overlying mantle wedge, via a Rayleigh-Taylor-like instability (Behn et al., 2011; Miller & Behn, 2012). Whether such diapirs melt within the core of the wedge, rise to the base of the crust, or penetrate the crust depends on their size and composition (e.g., Behn et al., 2011; Erdman & Lee, 2014; Kelemen & Behn, 2016).We consider in the companion paper which of the candidate rock types are likely to rise from the wedge-slab interface in this way.

6. Pressure-Temperature-Time Paths

We now turn to the pressure-temperature-time (P-T-t) paths that we should expect rocks to follow as they travel along the subduction interface. Temperatures on the plate interface are given by Equation 1 and, during motion down the plate interface, the prograde paths of rocks will follow P-T profiles similar to the profiles illustrated in Figure 8: once rocks are within the wedge-slab interface, their temperatures increase slowly with depth (Sections 4.1 and 4.2). The retrograde paths are dictated by the rate at which rocks of the interface rise through the differently evolving thermal regimes of plate and wedge-slab interfaces.

Figure 12 illustrates the temperature distributions near plate and slab-wedge interfaces during subduction, the evolution of those temperature profiles following cessation of subduction, and representative P-T-t paths. (See Appendix B for details of calculations.) During subduction, dissipative heating within the interface keeps temperatures higher there than in rocks above or below the interface (red line in Figure 12a), but once dissipation ceases the plate interface cools. In contrast, the wedge-slab interface is colder than the wedge above it, so that interface warms following the cessation of subduction (Figure 12b).

In each of the initial thermal profiles shown in Figures 12a and 12b there is an inverted thermal gradient at the interface that is approximately $T_f/\sqrt{\kappa t}$, where T_f is the temperature on the interface, and t is the time since the lower plate entered the trench (Equation 8). In Figure 12a, that time is approximately 3 Myr, and the region of inverted gradient is about 10 km thick. In Figure 12b, $t \sim 6$ Myr and the inverted gradient below the top of the interface is about 14 km thick; the region of inverted gradient in the wedge (Figure 12b) is of comparable

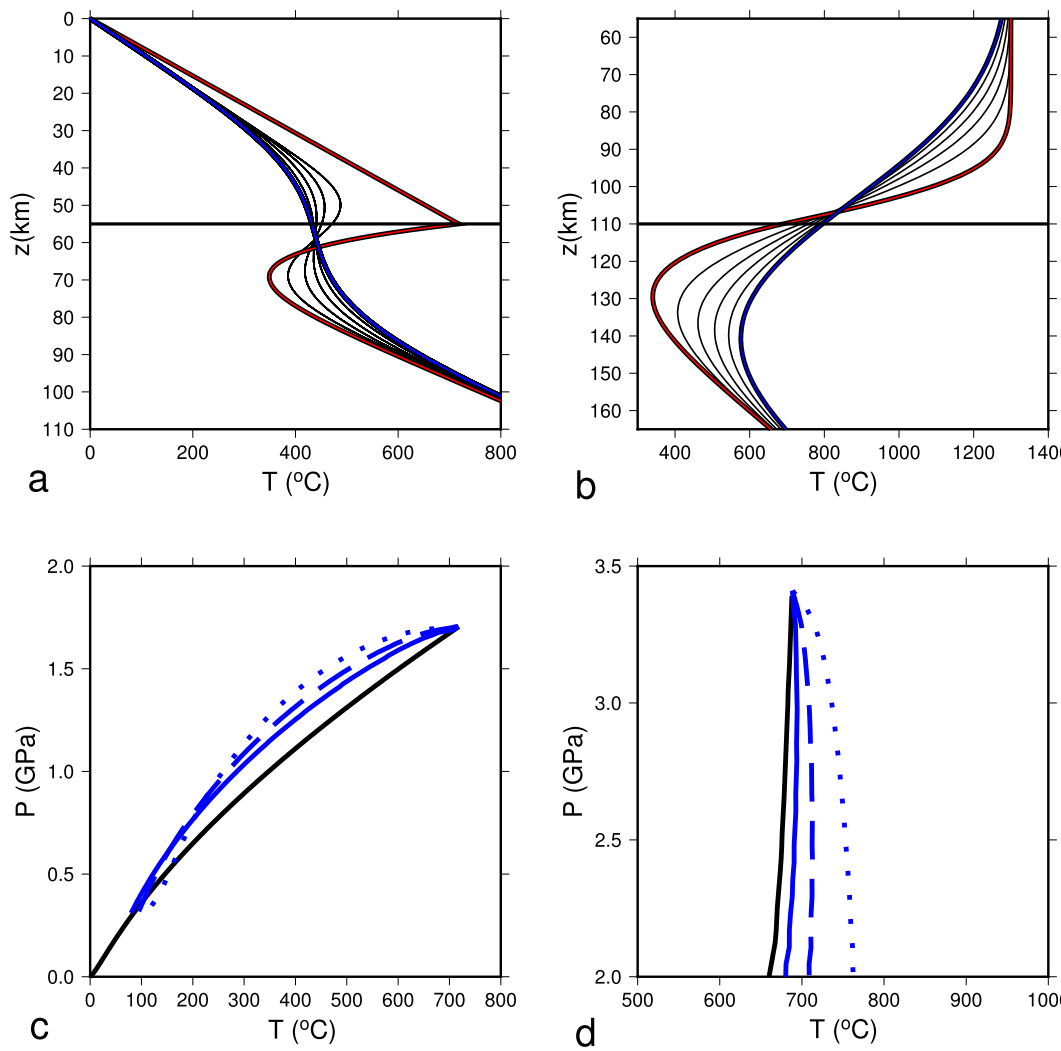

Figure 12. Illustrative thermal histories and P-T-t paths for plate and wedge-slab interfaces. (a and b) Thermal relaxation on profiles through the subduction interface following cessation of subduction. (a) Calculations for plate interface at depth 55 km with $V = 50$ mm/yr, $\delta = 20°$, $\mu' = 0.07$ and age of ocean floor 100 Myr. Red line corresponds to the steady temperature during subduction; black lines show temperature structure at 1-Myr intervals during thermal relaxation, up to 5 Myr (blue line). (b) Red line shows temperature profile 55 km above and below wedge-slab interface at a depth of 110 km; black lines show temperature structure at 2-Myr intervals during thermal relaxation, up to 10 Myr (blue line). (c) P-T-t path followed by rock originally buried to 55 km on the plate interface that is exhumed along the interface at 50 mm/yr (solid blue line) and at 1/3 and 1/10 that rate (dashed and dotted lines, respectively). (d) As (c), for rock initially buried at 110 km on the wedge-slab interface. See Appendix B for details of calculations.

thickness (Section 4.2). Once subduction ceases, thermal diffusion erases these inverted gradients over approximately the same time interval that they took to form (black lines in Figures 12a and 12b).

Figure 12c illustrates the P-T-t paths associated with the thermal history shown in Figure 12a. The black line shows the P-T conditions as the rock passes down the plate interface at a speed $V = 50$ mm/yr, with dissipative heating on the interface corresponding to an effective coefficient of friction $\mu' = 0.07$ (Equations 1–5). When the rock has reached a depth of 55 km (equivalent to ∼1.6 GPa) subduction ceases and the rock begins to ascend the interface. Three different return paths are illustrated, for ascent speeds of 50, 17, and 5 mm/yr; the thermal relaxation takes place principally in the first million years (Figure 12a), and the paths generally differ from each other by less than 100°C at any depth. Because dissipation on the interface has stopped, the retrograde path that the rock follows is cooler than the prograde path (except, in the example shown, for the slowest exhumation rate and at temperatures $\lesssim$150°C). For the slowest of these ascent rates, it is likely that P-T paths are also affected by changes in slab dynamics (Holt & Condit, 2021).

Figure 12d illustrates the P-T-t paths followed by a rock initially buried to 110 km on the wedge-slab interface, then exhumed at speeds of 50, 17, and 5 mm/yr. In contrast to rocks on the plate interface, these rocks are heated during their passage along the interface, as heat flows from the wedge into the lower plate (Figure 12b). In consequence, the P-T-t paths show slightly increasing temperatures during decompression, with greater temperature increases at slower exhumation rates.

The P-T-t paths for different ages of ocean floor and convergence rates will differ in detail from those illustrated here, but the principles will remain the same. Rocks buried and exhumed within the plate interface will cool after the cessation of shear heating, and their paths are likely to have the "hairpin" form shown in Figure 12c. In contrast, diffusion of heat from the wedge will maintain temperatures in the wedge-slab during exhumation. Therefore, the difference between P-T-t paths showing approximately isothermal decompression and those showing cooling during decompression may depend more upon their starting positions within the subduction interface than upon variation in tectonic setting of the subduction zone as a whole (cf., Agard et al., 2009; Ernst, 1988).

6.1. Influence of Earthquakes on P-T-t Paths

As discussed in Section 5.1, direct evidence of the thermal imprint of earthquakes, in the form of pseudotachylites or their altered remnants, is expected to be rare. The duration of heating is short (seconds) in comparison with likely time scales for the alteration of the pseudotachylites (perhaps a few days [e.g., Fondriest et al., 2020]) which, in turn, is short in comparison with the time between successive large earthquakes (hundreds or thousands of years).

We should, however, expect a distinctive imprint on P-T-t paths from the migration of fault planes within the interface (Section 5.1). Consider a unit that follows a prograde path within the interface similar to that in Figure 12c with the principal fault zone, on which the large and great earthquakes occur, being above it. Suppose that, at some point in the burial of this unit, the principal fault zone were to switch from being above to being beneath it. The unit would cool slightly (see Figure 12a), at constant pressure. Assuming that mineral growth terminates at this PT condition, we should expect metamorphic mineral geochronometers, such as the garnet Lu-Hf, garnet Sm-Nd and zircon and monazite (U/Th)-Pb systems, to preserve a record of the timing of the switch. In contrast, thermochronometers sensitive to thermally activated volume diffusion at temperatures relevant to the plate interface (300–600°C; see Figure 8), such as muscovite and amphibole $^{40}Ar/^{39}Ar$, and rutile and apatite U-Pb, would record the passage of individual isotopic systems through their closure temperatures—which may be delayed until the interface and its surroundings cool rapidly following the cessation of subduction (Figures 12a and 12c).

Given the hundreds of kilometers of convergence accommodated by large and great earthquakes across the plate-interface, it seems likely that the fault plane migrates repeatedly throughout the lifetime of a subduction zone. This process could assemble an imbricate stack of thrust sheets above the fault plane, each recording similar PT conditions and successively younger ages of migration and subsequent isobaric cooling. Such a framework draws empirical support from a number of regional-scale structural and metamorphic observations from exhumed HPLT terranes. Particular examples include the Cycladic Blueschist Unit (e.g., Kotowski et al., 2022; Ring et al., 2020), the Tavşanli zone (western Turkey) (e.g., Plunder et al., 2015), the southern Tianshan metamorphic belt (e.g., Bayet et al., 2018), the HPLT massifs of the Western Alps (e.g., Angiboust et al., 2011, 2012;

Reinecke, 1998; Smye et al., 2021; Starr et al., 2020) and the Raspas Complex of Ecuador (e.g., John et al., 2009). In each of these examples, stacking of thrust sheets occurred at ~2–3 GPa and 500–600°C over several millions of years.

The similarity of PT conditions within individual thrust sheets has led to postulation of a common depth of "detachment" or "decoupling" of slab-top material, caused by reaction-induced changes to interface rheology (e.g., Agard et al., 2018). We note that the length scales of exhumed HPLT terranes are generally small in comparison with the scales of fault planes on which large and great earthquakes occur (tens km downdip, hundreds km along-strike) so if, as suggested in Section 5.1.1, "detachment" is caused by earthquakes, this will be difficult to identify from field observations.

6.2. Repeated Burial and Exhumation

A small fraction of the P-T-t paths reported from HPLT terrains show evidence of more than one episode of burial and exhumation (e.g., Blanco-Quintero et al., 2011; J.-L. Li et al., 2016; Rubatto et al., 2011; Tamblyn et al., 2020). Some of these paths (e.g., J.-L. Li et al., 2016) appear to record a few kilobars of approximately isothermal decompression, followed by a P-T-t path that is consistent with later heating and exhumation within thickened crust, as we discuss in the companion paper (Smye & England, 2022). Others, however (e.g., Blanco-Quintero et al., 2011), are consistent with the circulation that might be expected within the plate interface if a rapid increase in sediment influx were to exceed the capacity of the interface (Shreve & Cloos, 1986, Figure 3).

Such P-T-t paths are sometimes explained by invoking circulation in an interface that is closed at its base (Cloos, 1982). This model is referred to as tectonic wedging (e.g., Maruyama et al., 1996) or extrusion (e.g., Beaumont et al., 2001). In its pure form, this scenario requires that all material entering the interface eventually returns to the surface, which is inconsistent with the observation that most sediments entering convergent margins are subducted (Clift & Vannucchi, 2004; Scholl & von Huene, 2007; von Huene and Scholl, 1991). Shreve and Cloos (1986) showed that, although the base of the interface should not close, there may nevertheless be circulation within the interface, depending upon sediment supply, interface capacity, and convergence rate (see also Cloos & Shreve, 1988a, 1988b). A re-investigation of the model of Shreve and Cloos (1986) with a wider range of values for their key parameters may provide further insights (cf., Gerya & Stöckhert, 2006).

7. Conclusions

Pressures and temperatures calculated from 281 analyses of rocks from HPLT terrains show that they represent two regimes: one, at pressures $\lesssim$1.5 GPa, in which temperature increases with pressure at about 350°C/GPa and one, at pressures above ~1.5 GPa, in which the temperatures are ~560 $\pm$ 80°C (Figure 1). The pressure of 1.5 GPa coincides with the modal maximum depth of thrust faulting in present-day subduction zones, and we interpret these two regimes as representing the plate interface and the wedge-slab interface. This distribution, which is seen both in HPLT thrust sheets and mélanges (Figure 2a), shows no difference between terrains that are interpreted as coming from ocean-ocean or from continent-ocean subduction zones (Figure 2b).

Using analytical expressions for temperatures along present-day plate interfaces (Section 3.2.1, England & May, 2021), we show that the observed distribution of data from pressures lower than 1.5–2 GPa is consistent with conditions on present-day plate interfaces constrained by measurements of surface heat flux (Figures 6 and 8, and Table 2, Section 4.1). This agreement provides detailed quantitative support for the contention of Penniston-Dorland et al. (2015) and Kohn et al. (2018) that geophysically reasonable rates of shear heating on the plate interface explain the difference between the metamorphic P-T data and some numerical models.

The low temperature gradients in the regime that we associate with the wedge-slab interface ($P \gtrsim 1.5$ GPa, Figure 1) is qualitatively consistent with scaling arguments about the temperature structure of the interface (Section 3.2.2, England & Katz, 2010; England & Wilkins, 2004). However, the observed temperatures themselves are lower than predicted by numerical calculations of temperatures at the top of the slab beneath the arc volcanoes (e.g., Syracuse et al., 2010) suggesting (Section 5.6) that the rocks of the wedge-slab interface, and of the wedge above it, have viscosities low enough to permit the buoyant ascent of diapirs (Behn et al., 2011; Miller & Behn, 2012) before sub-arc depths are reached.

Seismological and geodetic measurements at most subduction zones show that the relative motion between plates is accommodated predominantly in earthquakes. Thus, the principal mechanism by which sediments are carried to depth on plate interfaces is slip in great earthquakes. Migration of slip surfaces during subduction of the interface may lead to relationships that are referred to as accretion, underplating, or detachment (Section 5.1).

The magnitude of shear stresses (some tens of MPa) estimated for present-day plate boundaries considerably exceeds the buoyancy stresses, which are a few MPa for interface thicknesses of a few hundred meters to a few kilometers (Section 5.2, England & Holland, 1979; Shreve & Cloos, 1986). Therefore, the conditions for subduction of sediments to depths greater than the base of the plate interface are likely met in all present-day subduction zones, regardless of the mode of deformation within the interface (Section 5.3). These estimated shear stresses imply that the effective viscosity of interfaces in which the relative plate motion is accommodated by distributed flow, must be much higher ($\gtrsim 10^{19}$ Pa s: tens of MPa divided by strain rates of $\sim 10^{-14}$ to $\sim 10^{-11}$ s^{-1}, Section 5.1.1), than assumed in some previous analyses ($\sim 10^{17}$ Pa s (e.g., Shreve & Cloos, 1986, Section 5.3)). In the companion paper (Smye & England, 2022) we discuss the conditions under which different rock types within the interface are capable of sustaining these stresses.

The simplest explanation for exhumation of HPLT terrains is cessation of subduction (Section 5.4); we cannot rule out other mechanisms that have been proposed, but we do not support the invocation of processes that are common today to explain a phenomenon that is rare in the geological record. A key aspect of the ascent phase is that, because of variations of density and effective viscosity within the interface—hence in ascent rates—units of contrasting compositions and metamorphic histories will be juxtaposed (Section 5.5).

Rocks ascending within the wedge-slab interface will follow P-T-t paths of isothermal decompression, or slight heating; due to the cessation of dissipative heating when subduction stops, retrograde paths for rocks within the plate interface will be parallel to, but cooler than, their prograde paths, showing a "hairpin" form (Section 6).

Appendix A: PT Data

A1. Uncertainties in P-T Estimates

The P-T estimates we use in our compilation are derived from one of six techniques, each with different sources and magnitudes of systematic and epistemic uncertainty. It is beyond the scope of the paper to discuss these individually; rather, in this appendix we provide an illustration of the magnitudes of systematic and random uncertainties associated with PT estimates derived from mineral equilibria. Readers are referred to Hodges and McKenna (1987), Kohn and Spear (1991), and Powell and Holland (1994) for a comprehensive treatment of the issue.

Uncertainty on a P-T determination derived from the intersection of multiple mineral equilibria stems primarily from uncertainty in ΔH_R and $\ln K$, where ΔH_R is the enthalpy of reaction and $\ln K$ is the natural logarithm of the equilibrium constant of each reaction (Powell & Holland, 1994). By comparison, uncertainties in ΔS_R (entropy of reaction) and ΔV_R (volume of reaction) are small. Of these, $\ln K$ dominates the total uncertainty budget of P-sensitive equilibria used for barometry (e.g., Powell & Holland, 1988), originating from propagation of counting statistics through relevant (and uncertain) activity-composition models. Errors in $\ln K$ are correlated between reactions if the respective reactions involve any of the same mineral end-members; these correlations propagate through to correlations between the P-T positions of the reaction intersections according to the general error propagation equation:

$$\mathbf{V_y} = \mathbf{J V_x J^T} \tag{A1}$$

where, V_y is the covariance matrix of y, V_x is the covariance matrix of x and J is the Jacobian of y with respect to x.

Eclogites and blueschists present a particular challenge for thermobarometry. Pelitic metasediments at HPLT conditions can yield low-variance assemblages with restricted PT fields, favoring application of the pseudo-section approach (e.g., the garnet-chloritoid-kyanite assemblage; Smye et al., 2010). However, in the absence of hydrous phases such as amphibole and lawsonite, the assemblage: garnet + omphacite + phengite ± kyanite ± quartz is stable in mafic HPLT rocks over several hundred degrees and several tens of kbar. Given the relative strength of mafic eclogites and blueschists to metasediments, such rocks typically preserve higher fidelity records of HPLT

conditions; as such, it is worthwhile to investigate the uncertainties associated with P-T determination from such assemblages.

The example chosen to illustrate the magnitude of uncertainties associated with thermobarometry of mafic eclogites is sample 2544 from Hoschek (2007). This sample is a texturally equilibrated mafic eclogite from the Tauern Window, Eastern Alps, characterized by the peak assemblage: garnet + omphacite + kyanite + quartz and additionally, zoisite. Avoiding discussion of epistemic uncertainties related to choice of equilibrium mineral phases and compositions, Figure A1 shows the results of PT determinations using three different calibrations of reactions among mineral end-members: grossular, pyrope, almandine, diopside, hedenbergite, celadonite, Fe-celadonite, muscovite, kyanite and quartz.

The specific reactions used are:

$$\underset{\text{diopside}}{6CaMgSi_2O_6} + \underset{\text{muscovite}}{3KAl_2AlSiO_{10}(OH)_2} = \underset{\text{grossular}}{2Ca_3Al_2Si_3O_{12}} + \underset{\text{pyrope}}{Mg_3Al_2Si_3O_{12}} + \underset{\text{celadonite}}{3KAlMgSi_4O_{10}(OH)_2} \quad \text{(A2)}$$

$$\underset{\text{kyanite}}{2Al_2SiO_5} + \underset{\text{diopside}}{3CaMgSi_2O_6} = \underset{\text{grossular}}{Ca_3Al_2Si_3O_{12}} + \underset{\text{pyrope}}{Mg_3Al_2Si_3O_{12}} + \underset{\text{quartz/coesite}}{2SiO_2} \quad \text{(A3)}$$

$$\underset{\text{almandine}}{Fe_3Al_2(SiO_4)_3} + \underset{\text{muscovite}}{3KAl_2AlSiO_{10}(OH)_2} + \underset{\text{quartz/coesite}}{4SiO_2} = \underset{\text{Fe-celadonite}}{3KFeAlSi_4O_{10}(OH)_2} + \underset{\text{kyanite}}{4Al_2SiO_5} \quad \text{(A4)}$$

$$\underset{\text{muscovite}}{3KAl_2AlSiO_{10}(OH)_2} + \underset{\text{hedenbergite}}{6CaFeSi_2O_6} = \underset{\text{grossular}}{2Ca_3Al_2Si_3O_{12}} + \underset{\text{almandine}}{Fe_3Al_2(SiO_4)_3} + \underset{\text{Fe-celadonite}}{3KFeAlSi_4O_{10}(OH)_2} \quad \text{(A5)}$$

Each of the PT determinations presented in Figure A1 is calculated using the same set of mineral compositions (garnet 4, omphacite 9, phengite 14 from sample 2544 of Hoschek [2007]). PT determinations using the Holland and Powell (1998) and Krogh Ravna and Terry (2004) calibrations are similar, around 2.7 GPa and 600°C with 2σ uncertainties of ~0.2 GPa and ~80°C. Incorporation of Fe-bearing mineral end members (dashed ellipse) yields a higher-temperature PT estimate with a larger uncertainty ellipse (~3 kbar and ~80°C), likely reflecting the effects of post-peak diffusional re-equilibration or inaccuracies in the assumptions made to calculate Fe^{2+}/Fe^{3+} ratios of Fe-bearing phases. These three overlapping PT estimates are also in broad agreement with the pseudosection-derived PT estimate (gray polygon). The garnet-clinopyroxene-phengite barometer of Waters (1993) yields significantly higher pressure estimates, >3 GPa.

These calculations demonstrate that typical magnitudes of absolute error associated with equilibria-based thermobarometry applied to mafic HPLT rocks is of order ±0.2 GPa and ±50°C (2σ). In the example shown, this

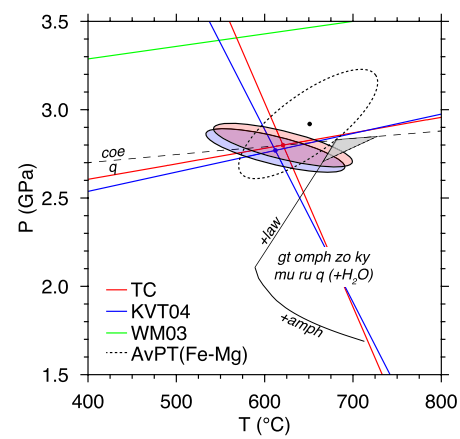

Figure A1. Thermobarometry of mafic eclogites: an illustration. Plot shows superimposed equilibria and error ellipses associated with three different calibrations of the garnet–clinopyroxene–phengite–kyanite–quartz/coesite thermobarometer applied to an Alpine eclogite (sample 2544 from Hoschek [2007]). The Krogh Ravna and Terry (2004) (blue line) and Holland and Powell (1998) database (red line) calibrations use Equation A2 and A3 whereas the Waters (1993) barometer (green line) uses Equation A2. The dashed error ellipse represents the PT estimate derived using the THERMOCALC average PT mode (Equations A2–A5) and the shaded polygon denotes the region of PT space defined by the peak mineral assemblage on a PT pseudosection calculated using the whole-rock bulk composition reported by Hoschek (2007).

dominates over the relative uncertainties between calibrations and, indeed, techniques. While the precision of the pseudosection-derived PT field is less than 0.2 GPa and 80°C, we emphasize that full propagation of geological uncertainties yields absolute magnitudes of uncertainty of similar order (e.g., Palin et al., 2016). Accordingly, we assume these values as minima in our compilation of HPLT data (Figure A2).

A2. Preservation of Peak HPLT Mineral Assemblages

Here we consider the implications of the P-T-t paths that HPLT terrains are likely to follow (Section 6) for the preservation of HPLT metamorphic mineral assemblages and the degree to which such mineral assemblages correspond to the maximum P and T attained along the path. The P-T conditions at which a metamorphic mineral assemblage is preserved are considered to reflect the point on a P-T-t path at which grain boundary fluid is removed from the rock (e.g., Fyfe, 2012; Fyfe et al., 1978; Walther & Orville, 1982), thus inhibiting further reaction.

Following the approach outlined by Guiraud et al. (2001), Figure A3 shows high-P segments of the P-T-t paths presented in Figure 12, superimposed on isopleths of bulk-rock weight percent H_2O in typical MORB and pelitic compositions. The large dP/dT characteristic of dehydration reactions means that rocks undergoing burial along the plate interface are expected to reach minimum bulk-rock H_2O contents at maximum depths of burial. As burial and dissipative heating are intrinsically linked, the cessation of burial and rapid onset of isobaric cooling moves plate interface rocks rapidly across isopleths of increasing bulk-rock H_2O content (Figures A3a and A3b). Assuming that (a) prograde fluids are lost from the rock volume and (b) the rock remains dry during exhumation, this analysis shows that—at least for pelitic and MORB-type compositions—estimates of maximum temperatures and pressures for plate interface rocks represent peak metamorphic conditions.

In contrast to the plate interface, rocks undergoing exhumation along the wedge-slab interface experience heating. For the pelite, this results in dehydration (and melting) during decompression, controlled by the breakdown of white mica (Figure A3c), and implies that exhumed HPLT metasediments may preserve a record of metamorphic conditions relevant to exhumation and not the true maximum burial depth associated with subduction. Bulk-rock H_2O contents for MORB at wedge-slab interface conditions are also controlled by the stability of white mica (Figure A3d), but notably, the isopleths are characterized by shallow dP/dT at sub-solidus conditions. This implies that mafic eclogites returned along the wedge-slab interface preserve a record of maximum pressure and temperature.

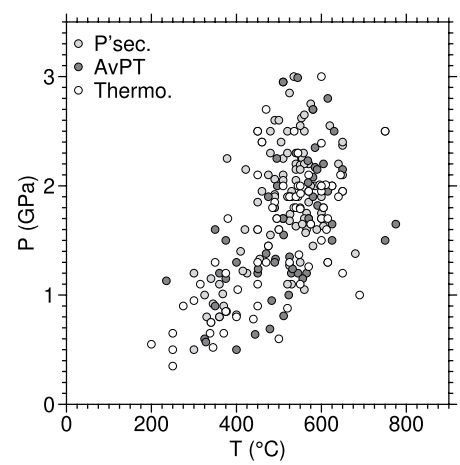

Figure A2. P-T data separated according to method of P-T determination. Shades indicate method of determination: P-T pseudo-sections (P'sec; light gray), average P-T method (AvPT; dark gray) and conventional thermobarometry (Thermo; open symbols). P-T estimates derived by Raman thermo/barometry, petrogenetic grids and single-phase solution thermometry are not shown here are because, combined, these methods account for <15% of the data set.

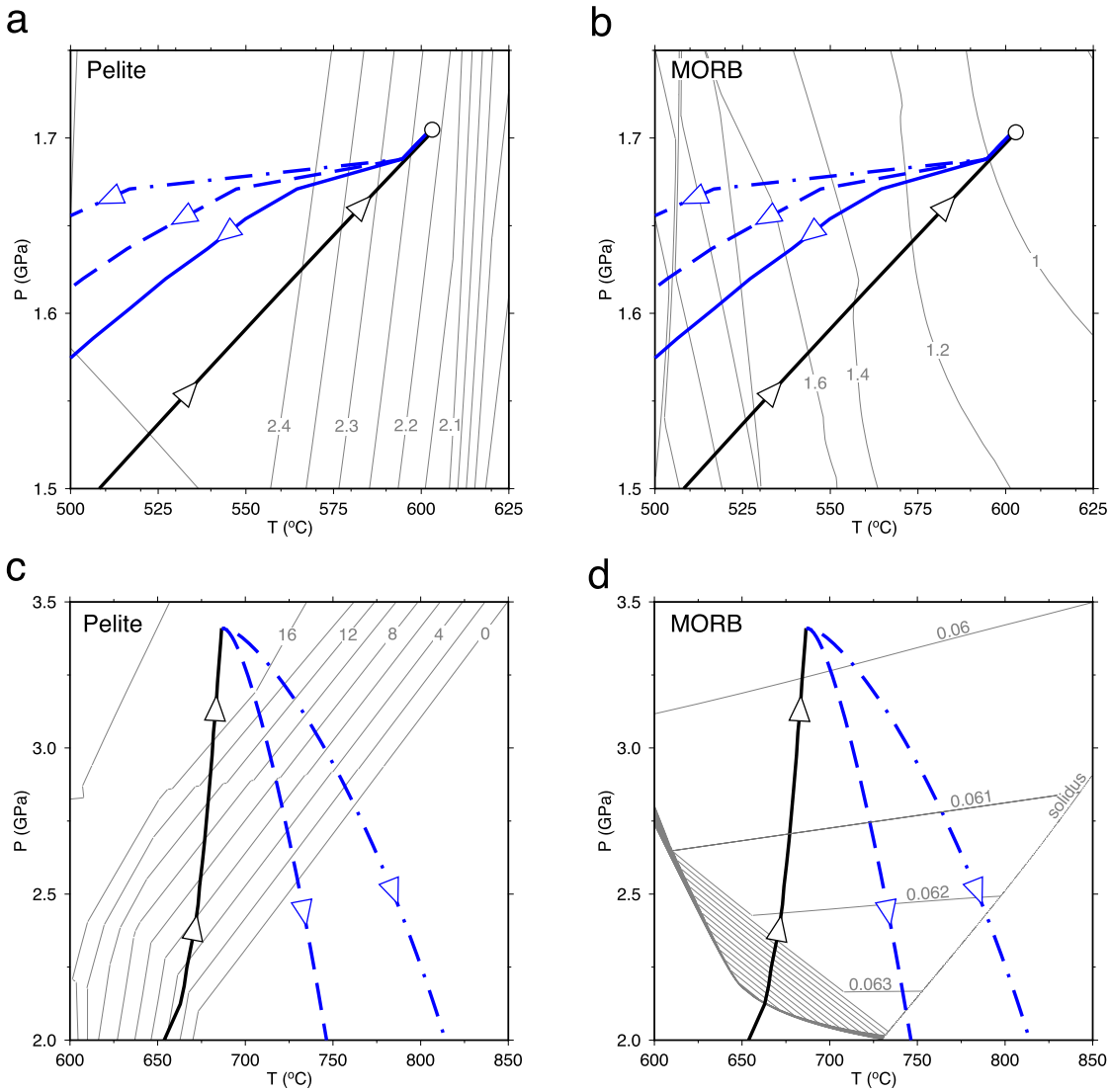

Figure A3. Relations between plate and wedge-slab interface P-T-t paths and bulk-rock H_2O contents. (a and b) P-T-t paths for the plate interface as shown in Figure 12, with contours of weight percent H_2O in solid mineral phases computed for a typical pelite and MORB, respectively. (c and d) As for (a and b) except for P-T-t paths along the wedge-slab interface and contours in (c) represent vol percent white mica–the only hydrous solid stable at conditions of interest (presented to avoid complications with H_2O in silicate melt). In each of the panels, arrowheads represent the direction of burial/exhumation a rock experiences; circles represent the point at which the P-T-t path is tangential to bulk-rock H_2O content and thus the P-T point corresponding the preserved mineral assemblage. See Appendix B for details of calculations.

Appendix B: Calculations of Wedge Temperatures and of P-T-t Paths

For the calculations illustrating P-T-t paths (Figure 12), we used the analytical expressions (Equations 1–5 and Equations 7–10) to set up the temperature profiles during subduction. We do this in preference to using numerical solutions so that readers may readily repeat the calculations for their own choices of parameters.

The initial temperature profile for the plate interface is calculated with convergence rate $V = 100$ mm/yr, dip $\delta = 25°$ and age of ocean floor 55 Myr. An effective coefficient of friction $\mu' = 0.07$ is used in Equation 1 to calculate temperature on the plate interface. For the wedge-slab interface (Figure 12b), we choose an illustrative value of $T_f = 680$°C for the syn-subduction temperature of the interface and T_w is taken to be 1300°C. This choice is somewhat higher than the temperature expected from the scaling arguments of Section 3.2.2, and is made for clarity of presentation of the retrograde paths; lower values of T_w give less heating during decompression. We

use $\beta = 15$ km in Equation 8, which is appropriate for the chosen depth and descent speed of the top of the lower plate. In this situation, heat flows from the wedge into the lower plate, while the temperature at the top of the lower plate changes little.

The thermal relaxation of the initial profiles shown in Figure 12 is calculated by the Crank-Nicolson finite-difference method (Crank, 1975) from the initial geotherms. All material is stationary; diffusion of heat parallel to the interface is ignored, as is the advection of heat by motion of the material of the subduction interface. The calculation domain extends from the surface, where temperature is fixed at 0°C, to the base of the lower plate, which is taken to be at a depth of 100 km below the interface, and is held at a temperature given by the heat flux, Q_0, through the lower plate.

Appendix C: Flow in the Subduction Interface

In this appendix we derive expressions for velocity distributions in a layer of power-law fluid confined between two parallel planes in the presence of a pressure gradient. In Appendices C1–C3 we derive expressions for fluids of constant physical properties then, in (Appendix C4), indicate the influence on the flow of temperature-dependent rheological properties. Appendix C5 discusses local thickening of the interface during ascent.

The layer has thickness h; the x-coordinate is in the down-dip direction and the y-coordinate is perpendicular to the layer, with its origin at the base of the layer. We express the rheology of the layer in the power-law form commonly used to describe laboratory measurements of the flow of rocks and minerals.

$$\dot{\varepsilon} = A f^r (\sigma_1 - \sigma_3)^n \exp\left(\frac{-E}{R\Theta}\right), \tag{C1}$$

where (usually) $\dot{\varepsilon}$ is the uniaxial shortening strain rate, σ_1 and σ_3 are the greatest and least principal compressional stresses, n is the power-law exponent, A is a material property, E is the activation energy for the deformation mechanism, Θ is absolute temperature, R is the gas constant, and f is the fugacity of H_2O.

Equation C1 may be re-cast in terms of the strain-rate and deviatoric-stress tensors (e.g., Molnar et al., 1998, Appendix):

$$\dot{\varepsilon}_{ij} = \frac{1}{2}\sqrt{3}^{(n+1)} A f^r \mathcal{T}^{(n-1)} \tau_{ij} \exp\left(\frac{-E}{R\Theta}\right) \tag{C2}$$

where $\dot{\varepsilon}_{ij}$ is the ijth component of the strain-rate tensor, τ_{ij} is the ijth component of the deviatoric stress, and

$$\mathcal{T} = \frac{1}{\sqrt{2}}(\tau_{kl}\tau_{kl})^{\frac{1}{2}} \tag{C3}$$

is the second invariant of the deviatoric stress tensor, with the convention of summation over repeated subscripts. With our assumed configuration of flow there is only one component of strain rate to consider, $\dot{\varepsilon}$, with its corresponding deviatoric stress, τ.

$$\dot{\varepsilon} = \frac{1}{2}\frac{dv}{dy}, \tag{C4}$$

$$\text{and } \tau = C\frac{dv}{dy}\left|\frac{dv}{dy}\right|^{1/n-1}, \tag{C5}$$

where, from Equations C1 and C5

$$C = \left(\frac{\exp(E/R\Theta)}{\sqrt{3}^{(n+1)} A f^r}\right)^{1/n}. \tag{C6}$$

Initially, we neglect variation of temperature across the interface, discussing the likely influence of such variations at the end of this subsection.

C1. Velocity Difference Between Top and Bottom of the Layer

Here we consider conditions relevant to the plate interface, taking the top of the layer to be fixed to the upper plate and its base to move at the speed of the lower plate ($v(h) = 0$, $v(0) = V$). Gerya and Stöckhert (2002) gave a solution of Equation 15 for $n = 3$. Complete solutions for higher integer values of n require the roots of quintic or higher polynomials, for which there are, in general, no algebraic expressions. Solutions can, however, be obtained for any positive value of n if the sign of the velocity does not change with depth in the layer.

If all the material of the layer of interest moves entirely in the $+x$-direction, the shear stress on top of the layer $\tau(h) \leq 0$ and $\frac{\mathrm{d}v}{\mathrm{d}y} \leq 0$ throughout the layer. We are interested in the case in which the layer is less dense than its surroundings ($\Phi > 0$); with v everywhere positive (down the layer), both sides of Equation 15 are always positive and we may write

$$\frac{\mathrm{d}v}{\mathrm{d}y}\left|\frac{\mathrm{d}v}{\mathrm{d}y}\right|^{(1/n-1)} = \frac{\Phi y}{C} - a \tag{C7}$$

$$\left|\frac{\mathrm{d}v}{\mathrm{d}y}\right|^{1/n} = a - \frac{\Phi y}{C} \tag{C8}$$

$$\left|\frac{\mathrm{d}v}{\mathrm{d}y}\right| = \left(a - \frac{\Phi y}{C}\right)^n \tag{C9}$$

$$\frac{\mathrm{d}v}{\mathrm{d}y} = -\left(\frac{a - \Phi y}{C}\right)^n, \tag{C10}$$

where a and b are constants of integration.

Let the shear stress on the top of the layer, $y = h$, be a negative multiple, $-\gamma$, of the buoyancy stress, Φh:

$$\tau(h) = -C\left|\frac{\mathrm{d}v}{\mathrm{d}y}\right|^{1/n}\Bigg|_h = -\gamma\Phi h, \tag{C11}$$

$$a = \frac{\Phi h\,(\gamma + 1)}{C}, \tag{C12}$$

$$\frac{\mathrm{d}v}{\mathrm{d}y} = -\left(\frac{\Phi}{C}\right)^n (h(1+\gamma) - y)^{n+1}, \tag{C13}$$

$$v = \frac{1}{(n+1)}\left(\frac{\Phi}{C}\right)^n (h(1+\gamma) - y)^{n+1} + b. \tag{C14}$$

On $y = h$, $v = 0$, hence

$$v = \frac{1}{(n+1)}\left(\frac{\Phi}{C}\right)^n \left[(h(1+\gamma) - y)^{n+1} - (h\gamma)^{n+1}\right]. \tag{C15}$$

The velocity on the base of the layer, V, is expressed in terms of the other parameters:

$$V = \frac{1}{(n+1)}\left(\frac{\Phi}{C}\right)^n \left[(h(1+\gamma))^{n+1} - (h\gamma)^{n+1}\right]. \tag{C16}$$

C2. Zero Velocity at Top and Bottom of the Layer

Here we give a solution for the dipping buoyant layer having velocity $v = 0$ on each boundary. In this case, $\mathrm{d}v/\mathrm{d}y$ changes sign in the middle of the layer and, because n is not necessarily an integer, we need—as in Appendix C1—to avoid dealing with non-integer powers of negative numbers. It is convenient to place $y = 0$ in the center of the layer and, making use of the condition

$$\left.\frac{\partial v}{\partial y}\right|_0 = 0, \tag{C17}$$

to solve for velocities in the half of the layer where both y and dv/dy are positive; the other half follows by symmetry.

With the boundary condition Equation C17 and Equation C10 becomes, for the half of the layer with dv/d$y > 0$,

$$\frac{\mathrm{d}v}{\mathrm{d}y} = \left(\frac{\Phi y}{C}\right)^n \tag{C18}$$

and with $v(h/2) = 0$

$$v = -\frac{h}{2(n+1)}\left(\frac{\Phi h}{2C}\right)^n \left(1 - \left(\frac{2y}{h}\right)^{n+1}\right). \tag{C19}$$

The full solution (Equation 19) differs from Equation C19 only in replacing y by its magnitude.

The maximum (upward) velocity in the layer is at $y = 0$

$$v_{\max} = -\frac{h}{2(n+1)}\left(\frac{\Phi h}{2C}\right)^n \tag{C20}$$

C3. Local Capacity of Layer

In the case of fixed velocity at top and base of the layer, the flux through the layer is, from Equation C15,

$$F = \int_0^h v\mathrm{d}y = Vh\left(\frac{\frac{1}{n+2}\left((1+\gamma)^{n+2} - \gamma^{n+2}\right) - \gamma^{n+1}}{(1+\gamma)^{n+1} - \gamma^{n+1}}\right), \tag{C21}$$

$$= \left[(n+1)\,V^{(n+2)}\left(\frac{C}{\Phi}\right)^n\right]^{1/(n+1)}\left(\frac{\frac{1}{n+2}\left((1+\gamma)^{n+2} - \gamma^{n+2}\right) - \gamma^{n+1}}{\left((1+\gamma)^{n+1} - \gamma^{n+1}\right)^{(n+2)/(n+1)}}\right), \tag{C22}$$

where we have substituted for h in Equation C21 from Equation C16. It may be shown, by the usual means of differentiating F with respect to γ, that the maximum of F is at $\gamma = 0$. (The algebra is not illuminating, so we omit it.) Thus the maximum flux is obtained when the shear stress on the top of the layer goes to zero ($\gamma = 0$) and the shear stress on its base is equal to the buoyancy stress, Φh. Then, Equation C15 reduces to

$$\lim_{\gamma\to 0}\frac{v}{V} = \left(1 - \frac{y}{h}\right)^{n+1} \tag{C23}$$

$$F_{\mathrm{local}} = \lim_{\gamma\to 0} F = \frac{1}{n+2}\left[(n+1)V^{(n+2)}\left(\frac{C}{\Phi}\right)^n\right]^{1/(n+1)}. \tag{C24}$$

For $n = 1$ these expressions reduce to those of Shreve and Cloos (1986).

Substituting for C (Equation C6) in Equation C24 gives the local capacity as

$$F_{\mathrm{local}} = \frac{1}{n+2}\left[\left(\frac{(n+1)V^{(n+2)}}{\Phi^n}\right)\left(\frac{\exp\left(E/R\Theta\right)}{\sqrt{3}^{(n+1)}Af^r}\right)\right]^{1/(n+1)}. \tag{C25}$$

If no material is added to or subtracted from the interface, then F_{local} represents the maximum flux of buoyant material entering the interface that can be accommodated at the depth of interest (Shreve & Cloos, 1986). Because of the variations in velocity profile with n and γ (Figures 9a–9c), the thickness, h, of interface required

to accommodate a given flux varies; when $\gamma \gtrsim 3$, however, the average speed in the interface is $\sim V/2$ (Figures 9b and 9c), so the local flux is $\sim Vh/2$. It is convenient to define the capacity in terms of an effective thickness

$$h_{\text{local}} = \frac{F_{\text{local}}}{V} = \frac{1}{n+2}\left[\frac{(n+1)V}{\Phi^n}\right]^{1/(n+1)}\left[\frac{\exp\left(E/R\Theta\right)}{\sqrt{3}^{(n+1)}Af^r}\right]^{1/(n+1)}. \tag{C26}$$

This thickness depends weakly on V is inversely proportional to Φ to a power close to one, and depends strongly on the physical properties of the interface material.

In the companion paper (Smye & England, 2022) we investigate the capacity for a wide range of rock types that are likely to be present in subduction interfaces;

C4. Influence of Temperature Variation Across the Interface

In this section we assess the influence on flow in the interface of the inverted temperature gradient associated with dissipative heating there. Duprat-Oualid et al. (2015) presented a dimensional analysis of the relative importance of the generation, diffusion, and advection of heat in major shear zones. We follow that analysis, with slight adaptations to the specifics of subduction interfaces.

Here, as established in the discussion of Section 3.2.1, we treat horizontal diffusion as negligible, and consider steady-state ($\partial\Theta/\partial t = 0$). The temperature equation is

$$\kappa\frac{\partial^2\Theta}{\partial z^2} - v\frac{\partial\Theta}{\partial x} + \frac{\tau}{\rho c}\frac{\mathrm{d}v}{\mathrm{d}z} = 0. \tag{C27}$$

From Equations 1–6, for high rates of convergence, V, and dissipative heating, τV, the thermal gradient across the interface is $\sim\tau V/K$. We consider a portion of interface, of thickness h, having absolute temperatures Θ_f at its top and $\Theta_f - \Delta\Theta$ at its base, where $\Delta\Theta$ scales as

$$\Delta\Theta \sim \tau V h/K. \tag{C28}$$

Dissipative heating is confined within the interface, so a natural non-dimensionalization is

$$\Theta = \Theta'\Delta\Theta \quad z = z'h; \quad v = v'V. \tag{C29}$$

Equation C27 becomes

$$\frac{Vh}{\kappa}\frac{\partial\Theta'}{\partial x'} = \frac{\partial^2\Theta'}{\partial z'^2} + \mathrm{Br}\frac{\mathrm{d}v'}{\mathrm{d}z'}, \tag{C30}$$

$$\mathrm{Br} = \frac{\tau Vh}{K\Delta\Theta}. \tag{C31}$$

Br is the Brinkman number, which expresses the relative importances of heat production and diffusion (e.g. Duprat-Oualid et al., 2015; Yuen et al., 1978). Because the thermal gradient across the interface, $\Delta\Theta/h, \approx \tau V/K$, Br is of order 1.

For typical convergence rates and interface thicknesses, Vh/κ is of order 1. Because temperature gradients along the interface are much smaller than those across the interface, $\partial\Theta'/\partial x' \ll 1$ and the left-hand side of Equation C30 may be neglected. Hence

$$\frac{\partial^2\Theta'}{\partial z'^2} \approx -\mathrm{Br}, \tag{C32}$$

where we recall, from Equation C29, that $\mathrm{d}v'/\mathrm{d}z' \sim 1$. This corresponds to the regime of Duprat-Oualid et al. (2015) in which mechanical dissipation and thermal diffusion have comparable influence (see their Figure 2). Curvature of the temperature gradient across the shear zone is modest, as shown by the calculations of Duprat-Oualid

et al. (2015, Figure 3) and Duprat-Oualid and Yamato (2017, Figure 1). For clarity, we therefore consider the mechanical impact of temperature dependence using a constant temperature gradient.

We consider a Newtonian fluid having the constitutive relation

$$\tau = \eta_0 \exp\left(\frac{E}{R\Theta}\right)\frac{\mathrm{d}v}{\mathrm{d}z}. \tag{C33}$$

With Equation C33, the stress-balance equation (Equation 15) becomes

$$\Phi = \frac{\mathrm{d}\tau}{\mathrm{d}z} \approx \eta_0 \exp\left(\frac{E}{R\Theta}\right)\left[\frac{\mathrm{d}^2 v}{\mathrm{d}z^2} - \frac{E}{R\Theta^2}\frac{\mathrm{d}\Theta}{\mathrm{d}z}\frac{\mathrm{d}v}{\mathrm{d}z}\right], \tag{C34}$$

$$\approx \eta_0 \exp\left(\frac{E}{R\Theta}\right)\left[\frac{\mathrm{d}^2 v}{\mathrm{d}z^2} - \frac{E}{R\Theta^2}\frac{\tau V}{K}\frac{\mathrm{d}v}{\mathrm{d}z}\right], \tag{C35}$$

where we have approximated $\mathrm{d}\Theta/\mathrm{d}z$ using Equation C28. Full solutions to this problem require numerical techniques (e.g., Yuen et al., 1978) and are beyond the scope of this paper. We may, however, assess the influence of temperature-dependent rheology on the flow through approximate solutions. The non-dimensional form of Equation C35 is

$$\frac{\mathrm{d}^2 v'}{\mathrm{d}z'^2} + E'\frac{\mathrm{d}v'}{\mathrm{d}z'} - \Psi \approx 0, \tag{C36}$$

where

$$E' = \frac{E\tau V h}{RK\Theta^2} = \mathrm{Br}\frac{E\Delta\Theta}{R\Theta^2}; \tag{C37}$$

$$\Psi = \frac{\Phi h^2}{V\eta_0 \exp\left(E/R\Theta\right)} \sim \frac{\Phi h}{\tau}. \tag{C38}$$

With $v'(0) = V$ and $v'(1) = V$, and holding Ψ constant,

$$v' = \frac{E'V\left(e^{E'} - e^{E'z}\right) - \Psi\left(ze^{E'} - e^{E'z} + (1-z)\right)}{\left(e^{E'} - 1\right)E'} \tag{C39}$$

Solutions for $\boldsymbol{\Psi} = 0$ are shown in Figure 9d, and for $V = 0$ in Figure 10a. As the temperature gradient across the interface goes to zero we recover the temperature-independent solutions for the velocity profiles:

$$\lim_{E'\to 0} v' = \left(V - \frac{\Psi z}{2}\right)(1-z) \tag{C40}$$

C5. Variations in Layer Thickness

If the thickness of the layer changes with time then mass conservation requires that

$$\frac{\partial h}{\partial t} = -\frac{\partial F}{\partial x} \tag{C41}$$

where F is the flux through the layer (Shreve & Cloos, 1986).

Our focus is on instability of the layer once subduction has ceased. A full analysis of this problem is beyond the scope of this paper; here we indicate only how such instabilities may arise, and estimate approximate time scales; see Ghosh et al. (2020) for further discussion. For simplicity, we consider a Newtonian fluid. We imagine a situation, immediately after the cessation of subduction, in which Φ and the layer thickness are both constant, but the viscosity of the layer varies with x. In particular, because the temperature of the layer increases with depth, we suppose

$$C = \eta(x) = \eta_0 \exp\left(\frac{-x}{\lambda}\right), \tag{C42}$$

where x is the distance (positive down-dip) from the location at which the viscosity is η_0, and λ is a scale length representing the temperature dependence of the viscosity and the temperature gradient down the layer.

When the velocities of top and bottom of the layer are the same, the flux through the layer in the $+x$ direction is, from Equation C19 with $n = 1$,

$$F = 2\int_0^{h/2} v\,\mathrm{d}y = -\frac{\Phi h^3}{12C}, \tag{C43}$$

and

$$\left.\frac{\partial h}{\partial t}\right|_{x=0} = \frac{\Phi h^3}{12\lambda\eta_0}. \tag{C44}$$

Here, we have assumed that, initially, h is constant in the region of interest. Equation C44 shows that, if viscosity of the layer decreases downwards, the layer will increase in thickness as material further down the layer moves more upwards. This process increases the thickness—hence buoyancy—of the layer at the point of interest increasing the upward flux there (Equation C43), leading to an instability in which the thickness of the layer, and the speed of ascent of material within it, both increase until they are limited by a phenomenon such as the highly viscous material more shallow in the layer and/or the perturbations in pressure arising from the instability. The time scale associated with the growth of such an instability is approximately

$$\frac{12\eta_0\lambda}{\Phi h_0^2}. \tag{C45}$$

We estimate λ by using variation in viscosity of a form commonly found in from laboratory experiments

$$\begin{aligned} \eta &= \eta_0 \exp\left(\frac{E}{RT}\right) \\ \frac{1}{\eta}\frac{\partial \eta}{\partial x} &= -\frac{1}{\lambda} = -\frac{E}{RT^2}\frac{\partial T}{\partial x} \\ \lambda &\sim \frac{RT^2}{EG} \end{aligned} \tag{C46}$$

where G is the temperature gradient along the interface and E is the activation energy for creep. With $G(\sim 10°\mathrm{C/km})$, E being a few times 10^5 kJ/mol for most minerals, and for temperatures of order 1000 K, $\lambda \sim 1$–10 km. With $\Phi \sim 1{,}000$ Pa/m, such instabilities will occur on time scales that are of order a million years or less, provided that $\eta_0 \lesssim 10^{19}$ Pa s.

Acknowledgments
This work was supported by the Natural Environment Research Council (NERC) through a Research Fellowship to AS, who also acknowledges support from the Slingerland Early Career endowment at Penn State University. PE is grateful for support from the Leverhulme Foundation. We thank Adam Holt, Peter Molnar, and John Platt for insightful comments on an earlier version of this manuscript. Two anonymous reviewers of that version alerted us to the need to explain the advantages of simple models, and the geophysical constraints upon them. The present manuscript benefitted from a helpful review by Thorsten Becker and from cogent editorial comments by Taras Gerya. Most figures were prepared using the GMT package (Wessel and Smith, 2013).

Data Availability Statement

All datasets supporting the conclusions in this paper are freely available online at this site: https://doi.org/10.17605/OSF.IO/JASV5.

References

Abers, G. A. (2005). Seismic low-velocity layer at the top of subducting slabs: Observations, predictions, and systematics. *Physics of the Earth and Planetary Interiors*, *149*(1–2), 7–29. https://doi.org/10.1016/j.pepi.2004.10.002

Abers, G. A., Van Keken, P. E., & Hacker, B. R. (2017). The cold and relatively dry nature of mantle forearcs in subduction zones. *Nature Geoscience*, *40*, 1–5. https://doi.org/10.1038/ngeo2922

Abers, G. A., van Keken, P. E., & Wilson, C. R. (2020). Deep decoupling in subduction zones: Observations and temperature limits. *Geosphere*, *16*(6), 1408–1424. https://doi.org/10.1130/GES02278.1

Agard, P., Plunder, A., Angiboust, S., Bonnet, G., & Ruh, J. (2018). The subduction plate interface: Rock record and mechanical coupling (from long to short timescales). *Lithos*, *320–321*, 537–566. https://doi.org/10.1016/j.lithos.2018.09.029

Agard, P., Yamato, P., Jolivet, L., & Burov, E. (2009). Exhumation of oceanic blueschists and eclogites in subduction zones: Timing and mechanisms. *Earth-Science Reviews*, *92*(1–2), 53–79. https://doi.org/10.1016/j.earscirev.2008.11.002

Andersen, T. B., Austrheim, H., Deseta, N., Silkoset, P., & Ashwal, L. D. (2014). Large subduction earthquakes along the fossil Moho in Alpine Corsica. *Geology*, *42*(5), 395–398. https://doi.org/10.1130/g35345.1

Angiboust, S., Agard, P., Raimbourg, H., Yamato, P., & Huet, B. (2011). Subduction interface processes recorded by eclogite-facies shear zones (Monviso, W. Alps). *Lithos*, *127*(1–2), 222–238. https://doi.org/10.1016/j.lithos.2011.09.004

Angiboust, S., Langdon, R., Agard, P., Waters, D., & Chopin, C. (2012). Eclogitization of the Monviso ophiolite (W. Alps) and implications on subduction dynamics. *Journal of Metamorphic Geology*, *30*(1), 37–61. https://doi.org/10.1111/j.1525-1314.2011.00951.x

Audet, P., Bostock, M. G., Christensen, N. I., & Peacock, S. M. (2009). Seismic evidence for overpressured subducted oceanic crust and megathrust fault sealing. *Nature*, *457*(7225), 76–78. https://doi.org/10.1038/nature07650

Audet, P., & Kim, Y. (2016). Teleseismic constraints on the geological environment of deep episodic slow earthquakes in subduction zone forearcs: A review. *Tectonophysics*, *670*, 1–15. https://doi.org/10.1016/j.tecto.2016.01.005

Batchelor, G. K. (1967). *An introduction to fluid dynamics*. Cambridge University Press.

Bayet, L., John, T., Agard, P., Gao, J., & Li, J.-L. (2018). Massive sediment accretion at 80 km depth along the subduction interface: Evidence from the southern Chinese Tianshan. *Geology*, *46*(6), 495–498. https://doi.org/10.1130/g40201.1

Beaumont, C., Jamieson, R., Nguyen, M., & Lee, B. (2001). Himalayan tectonics explained by extrusion of a low-viscosity crustal channel coupled to focused surface denudation. *Nature*, *414*(6865), 738–742. https://doi.org/10.1038/414738a

Bebout, G. E. (1995). The impact of subduction-zone metamorphism on mantle-ocean chemical cycling. *Chemical Geology*, *126*(2), 191–218. https://doi.org/10.1016/0009-2541(95)00118-5

Bebout, G. E., & Penniston-Dorland, S. C. (2016). Fluid and mass transfer at subduction interfaces—The field metamorphic record. *Lithos*, *240–243*, 228–258. https://doi.org/10.1016/j.lithos.2015.10.007

Behn, M. D., Kelemen, P. B., Hirth, G., Hacker, B. R., & Massonne, H.-J. (2011). Diapirs as the source of the sediment signature in arc lavas. *Nature Geoscience*, *4*(9), 641–646. https://doi.org/10.1038/ngeo1214

Behr, W. M., & Bürgmann, R. (2021). What's down there? The structures, materials and environment of deep-seated slow slip and tremor. *Philosophical Transactions of the Royal Society A: Mathematical, Physical & Engineering Sciences*, *379*(2193), 20200218. https://doi.org/10.1098/rsta.2020.0218

Ben-Zion, Y. (2017). On different approaches to modeling. *Journal of Geophysical Research: Solid Earth*, *122*(1), 558–559. https://doi.org/10.1002/2016jb013922

Beroza, G., & Ide, S. (2009). Deep tremors and slow quakes. *Science*, *324*(5930), 1025–1026. https://doi.org/10.1126/science.1171231

Bialas, R. W., Funiciello, F., & Faccenna, C. (2011). Subduction and exhumation of continental crust: Insights from laboratory models. *Geophysical Journal International*, *184*(1), 43–64. https://doi.org/10.1111/j.1365-246X.2010.04824.x

Bilek, S. L., & Lay, T. (2018). Subduction zone megathrust earthquakes. *Geosphere*, *14*(4), 1468–1500. https://doi.org/10.1130/GES01608.1

Blanco-Quintero, I. F., García-Casco, A., & Gerya, T. V. (2011). Tectonic blocks in serpentinite mélange (eastern Cuba) reveal large-scale convective flow of the subduction channel. *Geology*, *39*(1), 79–82. https://doi.org/10.1130/G31494.1

Brown, J. R., Beroza, G. C., Ide, S., Ohta, K., Shelly, D. R., Schwartz, S. Y., et al. (2009). Deep low-frequency earthquakes in tremor localize to the plate interface in multiple subduction zones. *Geophysical Research Letters*, *36*(19), 1–5. https://doi.org/10.1029/2009gl040027

Brown, J. R., Prejean, S. G., Beroza, G. C., Gomberg, J. S., & Haeussler, P. J. (2013). Deep low-frequency earthquakes in tectonic tremor along the Alaska-Aleutian subduction zone. *Journal of Geophysical Research-Solid Earth*, *118*(3), 1079–1090. https://doi.org/10.1029/2012jb009459

Brudzinski, M. R., Schlanser, K. M., Kelly, N. J., DeMets, C., Grand, S. P., Márquez-Azúa, B., & Cabral-Cano, E. (2016). Tectonic tremor and slow slip along the northwestern section of the Mexico subduction zone. *Earth and Planetary Science Letters*, *454*, 259–271. https://doi.org/10.1016/j.epsl.2016.08.004

Brune, J. N. (1968). Seismic moment, seismicity and rate of slip along major fault zones. *Journal of Geophysical Research*, *73*(2), 777–784. https://doi.org/10.1029/jb073i002p00777

Chatelain, J., Molnar, P., Prévot, R., & Isacks, B. (1992). Detachment of part of the downgoing slab and uplift of the New Hebrides (Vanuatu) Islands. *Geophysical Research Letters*, *19*(14), 1507–1510. https://doi.org/10.1029/92gl01389

Chen, T., & Clayton, R. W. (2009). Seismic attenuation structure in central Mexico: Image of a focused high-attenuation zone in the mantle wedge. *Journal of Geophysical Research*, *114*(B7), B07304. https://doi.org/10.1029/2008JB005964

Christensen, N. I. (2004). Serpentinites, peridotites, and seismology. *International Geology Review*, *46*(9), 795–816. https://doi.org/10.2747/0020-6814.46.9.795

Clift, P., & Vannucchi, P. (2004). Controls on tectonic accretion versus erosion in subduction zones: Implications for the origin and recycling of the continental crust. *Reviews of Geophysics*, *42*(2), RG2001. https://doi.org/10.1029/2003rg000127

Cloos, M. (1982). Flow melanges: Numerical modeling and geologic constraints on their origin in the Franciscan subduction complex, California. *The Geological Society of America Bulletin*, *93*(4), 330. https://doi.org/10.1130/0016-7606(1982)93<330:fmnmag>2.0.co;2

Cloos, M. (1983). Comparative study of melange matrix and metashales from the Franciscan subduction complex with the basal Great Valley sequence, California. *The Journal of Geology*, *91*(3), 291–306. https://doi.org/10.1086/628772

Cloos, M., & Shreve, R. (1988a). Subduction-channel model of prism accretion, melange formation, sediment subduction, and subduction erosion at convergent plate margins: 1. Background and description. *Pure and Applied Geophysics*, *128*(3–4), 455–500. https://doi.org/10.1007/bf00874548

Cloos, M., & Shreve, R. L. (1988b). Subduction-channel model of prism Accretion, melange formation, sediment subduction, and subduction erosion at convergent plate margins: 2. Implications and discussion. *Pure and Applied Geophysics*, *128*(3–4), 501–545. https://doi.org/10.1007/bf00874549

Coleman, R., Lee, D., Beatty, L., & Brannock, W. W. (1965). Eclogites and eclogites: Their differences and similarities. *The Geological Society of America Bulletin*, *76*(5), 483–508. https://doi.org/10.1130/0016-7606(1965)76[483:eaetda]2.0.co;2

Coleman, R. G. (1971). Petrologic and geophysical nature of serpentinites. *The Geological Society of America Bulletin*, *82*(4), 897. https://doi.org/10.1130/0016-7606(1971)82[897:pagnos]2.0.co;2

Cowan, D. (1999). Do faults preserve a record of seismic slip? A field geologist's opinion. *Journal of Structural Geology*, *21*(8–9), 995–1001. https://doi.org/10.1016/s0191-8141(99)00046-2

Crank, J. (1975). *The mathematics of diffusion* (2nd ed.). Oxford University Press.

Croon, M. B., Cande, S. C., & Stock, J. M. (2008). Revised Pacific-Antarctic plate motions and geophysics of the Menard Fracture Zone. *Geochemistry, Geophysics, Geosystems*, *9*(7). https://doi.org/10.1029/2008GC002019

DeMets, C., & Merkouriev, S. (2019). High-resolution reconstructions of south America plate motion relative to Africa, Antarctica and North America: 34 Ma to present. *Geophysical Journal International*, *217*(3), 1821–1853. https://doi.org/10.1093/gji/ggz087

DeMets, C., & Merkouriev, S. (2021). Detailed reconstructions of India-Somalia plate motion, 60 Ma to present: Implications for Somalia plate absolute motion and India-Eurasia plate motion. *Geophysical Journal International*, *227*(3), 1730–1767. https://doi.org/10.1093/gji/ggab295

Demets, C., Merkouriev, S., & Sauter, D. (2015). High-resolution estimates of Southwest Indian Ridge plate motions, 20 Ma to present. *Geophysical Journal International*, *203*(3), 1495–1527. https://doi.org/10.1093/gji/ggv366

Duprat-Oualid, S., & Yamato, P. (2017). On the meaning of peak temperature profiles in inverted metamorphic sequences. *Geophysical Journal International*, *210*(1), 130–147. https://doi.org/10.1093/gji/ggx129
Duprat-Oualid, S., Yamato, P., & Schmalholz, S. M. (2015). A dimensional analysis to quantify the thermal budget around lithospheric-scale shear zones. *Terra Nova*, *27*(3), 163–168. https://doi.org/10.1111/ter.12144
Dyson, F. (2004). A meeting with Enrico Fermi. *Nature*, *427*(6972), 297. https://doi.org/10.1038/427297a
Dziewonski, A., & Anderson, D. (1981). Preliminary reference Earth model. *Physics of the Earth and Planetary Interiors*, *25*(4), 297–356. https://doi.org/10.1016/0031-9201(81)90046-7
Eberhart-Phillips, D., Bannister, S., & Reyners, M. (2020). Attenuation in the mantle wedge beneath super-volcanoes of the Taupo Volcanic Zone, New Zealand. *Geophysical Journal International*, *220*(1), 703–723. https://doi.org/10.1093/gji/ggz455
Elliott, T., Plank, T., Zindler, A., White, W., & Bourdon, B. (1997). Element transport from slab to volcanic front at the Mariana Arc. *Journal of Geophysical Research*, *102*(B7), 14991–15020. https://doi.org/10.1029/97jb00788
England, P., & Holland, T. (1979). Archimedes and the Tauern eclogites: The role of buoyancy in the preservation of exotic eclogite blocks. *Earth and Planetary Science Letters*, *44*(2), 287–294. https://doi.org/10.1016/0012-821x(79)90177-8
England, P., & Molnar, P. (1990). Surface uplift, uplift of rocks, and exhumation of rocks. *Geology*, *18*(12), 1173–1177. https://doi.org/10.1130/0091-7613(1990)018<1173:suuora>2.3.co;2
England, P., & Wilkins, C. (2004). A simple analytical approximation to the temperature structure in subduction zones. *Geophysical Journal International*, *159*(3), 1138–1154. https://doi.org/10.1111/j.1365-246x.2004.02419.x
England, P. C. (2018). On shear stresses and the maximum magnitudes of earthquakes at convergent plate boundaries. *Journal of Geophysical Research: Solid Earth*, *123*, 7165–7202. https://doi.org/10.1029/2018JB015907
England, P. C., & Katz, R. F. (2010). Melting above the anhydrous solidus controls the location of volcanic arcs. *Nature*, *467*(7316), 700–703. https://doi.org/10.1038/nature09417
England, P. C., & May, D. A. (2021). The global range of temperatures on convergent plate interfaces. *Geochemistry, Geophysics, Geosystems*, *22*(8), e2021GC009849. https://doi.org/10.1029/2021GC009849
Erdman, M. E., & Lee, C.-T. A. (2014). Oceanic- and continental-type metamorphic terranes: Occurrence and exhumation mechanisms. *Earth-Science Reviews*, *139*, 33–46. https://doi.org/10.1016/j.earscirev.2014.08.012
Ernst, W. (1975). Systematics of large-scale tectonics and age progressions in Alpine and Circum-Pacific blueschist belts. *Tectonophysics*, *26*(3–4), 229–246. https://doi.org/10.1016/0040-1951(75)90092-X
Ernst, W. (1993). Metamorphism of Franciscan tectonostratigraphic assemblage, Pacheco Pass area, east-central Diablo Range, California coast ranges. *The Geological Society of America Bulletin*, *105*(5), 618–636. https://doi.org/10.1130/0016-7606(1993)105<0618:moftap>2.3.co;2
Ernst, W. G. (1970). Tectonic contact between the Franciscan mélange and the Great Valley sequence – Crustal expression of a late Mesozoic Benioff zone. *Journal of Geophysical Research*, *75*(5), 886–901. https://doi.org/10.1029/jb075i005p00886
Ernst, W. G. (1971). Do mineral parageneses reflect unusually high-pressure conditions of Franciscan metamorphism? *American Journal of Science*, *270*(2), 81–108. https://doi.org/10.2475/ajs.270.2.81
Ernst, W. G. (1973). Blueschist metamorphism and P-T regimes in active subduction zones. *Tectonophysics*, *17*(3), 255–272. https://doi.org/10.1016/0040-1951(73)90006-1
Ernst, W. G. (1988). Tectonic history of subduction zones inferred from retrograde blueschist P-T paths. *Geology*, *16*(12), 1081. https://doi.org/10.1130/0091-7613(1988)016<1081:thoszi>2.3.co;2
Ernst, W. G., Maruyama, S., & Wallis, S. (1997). Buoyancy-driven, rapid exhumation of ultrahigh-pressure metamorphosed continental crust. *Proceedings of the National Academy of Sciences of the United States of America*, *94*(18), 9532–9537. https://doi.org/10.1073/pnas.94.18.9532
Fagereng, A., & Sibson, R. H. (2010). Melange rheology and seismic style. *Geology*, *38*(8), 751–754. https://doi.org/10.1130/g30868.1
Fagereng, A., & Toy, V. G. (2011). Geology of the earthquake source: An introduction. *Geological Society London Special Publications*, *359*, 1–16. https://doi.org/10.1144/sp359.1
Fondriest, M., Mecklenburgh, J., Passelegue, F. X., Artioli, G., Nestola, F., Spagnuolo, E., et al. (2020). Pseudotachylyte alteration and the rapid fade of earthquake scars from the geological record. *Geophysical Research Letters*, *47*(22). https://doi.org/10.1029/2020GL090020
Fyfe, W., Price, N., & Thompson, A. (1978). *Fluids in the Earth's crust* (p. 383). Elsevier.
Fyfe, W. S. (2012). *Fluids in the Earth's crust: Their significance in metamorphic, tectonic and chemical transport process* (Vol. 1). Elsevier.
Gao, X., & Wang, K. (2014). Strength of stick-slip and creeping subduction megathrusts from heat flow observations. *Science*, *345*(6200), 1038–1041. https://doi.org/10.1126/science.1255487
Garzanti, E., Radeff, G., & Malusà, M. G. (2018). Slab breakoff: A critical appraisal of a geological theory as applied in space and time. *Earth-Science Reviews*, *177*, 303–319. https://doi.org/10.1016/j.earscirev.2017.11.012
Gerya, T., & Stöckhert, B. (2006). Two-dimensional numerical modeling of tectonic and metamorphic histories at active continental margins. *International Journal of Earth Sciences*, *95*(2), 250–274. https://doi.org/10.1007/s00531-005-0035-9
Gerya, T. V., & Stöckhert, B. (2002). Exhumation rates of high pressure metamorphic rocks in subduction channels: The effect of rheology. *Geophysical Research Letters*, *29*(8), 1021–1024. https://doi.org/10.1029/2001GL014307
Gerya, T. V., Stöckhert, B., & Perchuk, A. L. (2002). Exhumation of high-pressure metamorphic rocks in a subduction channel: A numerical simulation. *Tectonics*, *21*(6), 6-1–6-19. https://doi.org/10.1029/2002tc001406
Ghosh, D., Maiti, G., & Mandal, N. (2020). Slab-parallel advection versus Rayleigh-Taylor instabilities in melt-rich layers in subduction zones: A criticality analysis. *Physics of the Earth and Planetary Interiors*, *307*, 106560. https://doi.org/10.1016/j.pepi.2020.106560
Greenberg, S. A. (2009). How citation distortions create unfounded authority: Analysis of a citation network. *BMJ*, *339*, b2680. https://doi.org/10.1136/bmj.b2680
Guillot, S., Hattori, K., Agard, P., Schwartz, S., & Vidal, O. (2009). Exhumation processes in oceanic and continental subduction contexts: A review. In S. Lallemand & F. Funiciello (Eds.), *Subduction zone geodynamics*. Springer-Verlag Berlin Heidelberg. https://doi.org/10.1007/978-3-540-87974-9
Guiraud, M., Powell, R., & Rebay, G. (2001). H_2O in metamorphism and unexpected behaviour in the preservation of metamorphic mineral assemblages. *Journal of Metamorphic Geology*, *19*(4), 445–454. https://doi.org/10.1046/j.0263-4929.2001.00320.x
Hacker, B. R. (2008). H_2O subduction beyond arcs. *Geochemistry, Geophysics, Geosystems*, *9*(3), 24. https://doi.org/10.1029/2007gc001707
Hawkesworth, C., Gallagher, K., & Hergt, J. (1993). Mantle and slab contributions in arc magmas. *Annual Review of Earth and Planetary Sciences*.
Hawkesworth, C. J., Hergt, J., Ellam, R., & McDermott, F. (1991). Element fluxes associated with subduction related magmatism. *Philosophical Transactions of the Royal Society of London. Series A: Physical and Engineering Sciences*, *335*, 393–405.
Hayes, G. P., Moore, G. L., Portner, D. E., Hearne, M., Flamme, H., Furtney, M., & Smoczyk, G. M. (2018). Slab2, a comprehensive subduction zone geometry model. *Science*, *362*(6410), 58–61. https://doi.org/10.1126/science.aat4723

Hayes, G. P., Wald, D. J., & Johnson, R. L. (2012). Slab1.0: A three-dimensional model of global subduction zone geometries. *Journal of Geophysical Research*, *117*(B01), 302. https://doi.org/10.1029/2011jb008524
Hermann, J., Müntener, O., & Scambelluri, M. (2000). The importance of serpentinite mylonites for subduction and exhumation of oceanic crust. *Tectonophysics*, *327*(3–4), 225–238. https://doi.org/10.1016/S0040-1951(00)00171-2
Heuret, A., Lallemand, S., Funiciello, F., Piromallo, C., & Faccenna, C. (2011). Physical characteristics of subduction interface type seismogenic zones revisited. *Geochemistry, Geophysics, Geosystems*, *12*(1), Q01004. https://doi.org/10.1029/2010GC003230
Heuret, A., Losq, J., & Lallemand, S. (2017). Submap: A tool for mapping subduction zones. Retrieved from http://submap.gm.univ-montp2.fr/index.php
Hirth, G., Teyssier, C., & Dunlap, J. (2001). An evaluation of quartzite flow laws based on comparisons between experimentally and naturally deformed rocks. *International Journal of Earth Sciences*, *90*(1), 77–87. https://doi.org/10.1007/s005310000152
Hodges, K., & McKenna, L. (1987). Realistic propagation of uncertainties in geologic thermobarometry. *American Mineralogist*, *72*, 671–680.
Holland, T., & Powell, R. (1998). An internally consistent thermodynamic data set for phases of petrological interest. *Journal of Metamorphic Geology*, *16*(3), 309–343. https://doi.org/10.1111/j.1525-1314.1998.00140.x
Holt, A. F., & Condit, C. B. (2021). Slab temperature evolution over the lifetime of a subduction zone. *Geochemistry, Geophysics, Geosystems*, *22*(6), e2020GC009476. https://doi.org/10.1029/2020GC009476
Hoschek, G. (2007). Metamorphic peak conditions of eclogites in the Tauern Window, Eastern Alps, Austria: Thermobarometry of the assemblage garnet+ omphacite+ phengite+ kyanite+ quartz. *Lithos*, *93*(1–2), 1–16. https://doi.org/10.1016/j.lithos.2006.03.042
Huet, B., Yamato, P., & Grasemann, B. (2014). The minimized power geometric model: An analytical mixing model for calculating polyphase rock viscosities consistent with experimental data. *Journal of Geophysical Research: Solid Earth*, *119*(4), 3897–3024. https://doi.org/10.1002/2013JB010453
Husson, L., Brun, J.-P., Yamato, P., & Faccenna, C. (2009). Episodic slab rollback fosters exhumation of HP–UHP rocks. *Geophysical Journal International*, *179*(3), 1292–1300. https://doi.org/10.1111/j.1365-246X.2009.04372.x
Ide, S., & Yabe, S. (2014). Universality of slow earthquakes in the very low frequency band. *Geophysical Research Letters*, *41*(8), 2786–2793. https://doi.org/10.1002/2014gl059712
Ikesawa, E., Sakaguchi, A., & Kimura, G. (2003). Pseudotachylyte from an ancient accretionary complex: Evidence for melt generation during seismic slip along a master décollement? *Geology*, *31*(7), 637–640. https://doi.org/10.1130/0091-7613(2003)031<0637:pfaaac>2.0.co;2
Isacks, B., Oliver, J., & Sykes, L. (1968). Seismology and the new global tectonics. *Journal of Geophysical Research*, *73*(5–6), 5855–5899. https://doi.org/10.1016/0040-1951(69)90024-9
Jarrard, R. D. (1986). Relations among subduction parameters. *Reviews of Geophysics*, *24*(2), 217–284. https://doi.org/10.1029/rg024i002p00217
John, T., & Schenk, V. (2006). Interrelations between intermediate-depth earthquakes and fluid flow within subducting oceanic plates: Constraints from eclogite facies pseudotachylytes. *Geology*, *34*(7), 557–564. https://doi.org/10.1130/g22411.1
John, T., Scherer, E. E., Schenk, V., Herms, P., Halama, R., & Garbe-Schönberg, D. (2009). Subducted seamounts in an eclogite-facies ophiolite sequence: The Andean Raspas Complex, SW Ecuador. *Contributions to Mineralogy and Petrology*, *159*(2), 265–284. https://doi.org/10.1007/s00410-009-0427-0
Kanamori, H., & Rivera, L. (2006). Energy partitioning during an earthquake. In R. Abercrombie, A. McGarr, G. D. Toro, & H. Kanamori (Eds.), *Earthquakes: Radiated energy and the physics of faulting*, *Geophysical Monograph Series* (Vol. 170, pp. 3–15). American Geophysical Union.
Karato, S., & Wu, P. (1993). Rheology of the upper mantle: A synthesis. *Science*, *260*(5109), 771–778. https://doi.org/10.1126/science.260.5109.771
Kato, A., Iidaka, T., Ikuta, R., Yoshida, Y., Katsumata, K., Iwasaki, T., et al. (2010). Variations of fluid pressure within the subducting oceanic crust and slow earthquakes. *Geophysical Research Letters*, *37*(14), L14310. https://doi.org/10.1029/2010gl043723
Kelemen, P. B., & Behn, M. D. (2016). Formation of lower continental crust by relamination of buoyant arc lavas and plutons. *Nature Geoscience*, *9*(3), 197–205. https://doi.org/10.1038/ngeo2662
Kerrick, D., & Connolly, J. (2001). Metamorphic devolatilization of subducted marine sediments and the transport of volatiles into the Earth's mantle. *Nature*, *411*(6835), 293–296. https://doi.org/10.1038/35077056
Keyser, W., Tsai, C.-H., Iizuka, Y., Oberhänsli, R., & Ernst, W. (2016). High-pressure metamorphism in the Chinshuichi area, Yuli belt, eastern Taiwan. *Tectonophysics*, *692*, 191–202. https://doi.org/10.1016/j.tecto.2015.09.012
Kim, Y., Abers, G. A., Li, J., Christensen, D., Calkins, J., & Rondenay, S. (2014). Alaska Megathrust 2: Imaging the megathrust zone and Yakutat/Pacific plate interface in the Alaska subduction zone. *Journal of Geophysical Research: Solid Earth*, *119*(3), 1924–1941. https://doi.org/10.1002/2013JB010581
Kim, Y., Miller, M. S., Pearce, F., & Clayton, R. W. (2012). Seismic imaging of the Cocos plate subduction zone system in central Mexico. *Geochemistry, Geophysics, Geosystems*, *13*(7), Q07001. https://doi.org/10.1029/2012gc004033
Kimura, G., & Ludden, J. (1995). Peeling oceanic crust in subduction zones. *Geology*, *23*(3), 217. https://doi.org/10.1130/0091-7613
Kirkpatrick, J. D., & Rowe, C. D. (2013). Disappearing ink: How pseudotachylytes are lost from the rock record. *Journal of Structural Geology*, *52*, 183–198. https://doi.org/10.1016/j.jsg.2013.03.003
Kirkpatrick, J. D., Shipton, Z. K., & Persano, C. (2009). Pseudotachylytes: Rarely generated, rarely preserved, or rarely reported? *Bulletin of the Seismological Society of America*, *99*(1), 382–388. https://doi.org/10.1785/0120080114
Kita, S., Nakajima, J., Hasegawa, A., Okada, T., Katsumata, K., Asano, Y., & Kimura, T. (2014). Detailed seismic attenuation structure beneath Hokkaido, northeastern Japan: Arc-arc collision process, arc magmatism, and seismotectonics. *Journal of Geophysical Research: Solid Earth*, *119*(8), 6486–6511. https://doi.org/10.1002/2014JB011099
Kohn, M. J., Castro, A. E., Kerswell, B. C., Ranero, C. R., & Spear, F. S. (2018). Shear heating reconciles thermal models with the metamorphic rock record of subduction. *Proceedings of the National Academy of Sciences of the United States of America*, *115*(46), 11706–11711. https://doi.org/10.1073/pnas.1809962115
Kohn, M. J., & Spear, F. S. (1991). Error propagation for barometers: 2. Application to rocks. *American Mineralogist*, *76*, 138–147.
Kotowski, A. J., Cisneros, M., Behr, W. M., Stockli, D. F., Soukis, K., Barnes, J. D., & Ortega-Arroyo, D. (2022). Subduction, underplating, and return flow recorded in the Cycladic Blueschist Unit exposed on Syros, Greece. *Tectonics*, *41*(6). https://doi.org/10.1029/2020TC006528
Krogh Ravna, E., & Terry, M. P. (2004). Geothermobarometry of uhp and hp eclogites and schists–an evaluation of equilibria among garnet–clinopyroxene–kyanite–phengite–coesite/quartz. *Journal of Metamorphic Geology*, *22*(6), 579–592. https://doi.org/10.1111/j.1525-1314.2004.00534.x
Krohe, A. (2017). The Franciscan Complex (California, USA) – The model case for return-flow in a subduction channel put to the test. *Gondwana Research*, *45*, 282–307. https://doi.org/10.1016/j.gr.2017.02.003
Kurz, W., Neubauer, F., & Dachs, E. (1998). Eclogite meso-and microfabrics: Implications for the burial and exhumation history of eclogites in the Tauern Window (Eastern Alps) from P-T-d paths. *Tectonophysics*, *285*(1–2), 183–209. https://doi.org/10.1016/s0040-1951(97)00188-1

Le Pichon, X. (1982). Land-locked oceanic basins and continental collision: The Eastern Mediterranean as a case example. In K. Hsü (Ed.), *Mountain building processes* (pp. 129–146). Academic Press.
Li, J.-L., Klemd, R., Gao, J., & John, T. (2016). Poly-cyclic metamorphic evolution of eclogite: Evidence for multistage burial–exhumation cycling in a subduction channel. *Journal of Petrology*, *57*(1), 119–146. https://doi.org/10.1093/petrology/egw002
Li, Z. H., Xu, Z. Q., & Gerya, T. V. (2011). Flat versus steep subduction: Contrasting modes for the formation and exhumation of high- to ultrahigh-pressure rocks in continental collision zones. *Earth and Planetary Science Letters*, *301*(1–2), 65–77. https://doi.org/10.1016/j.epsl.2010.10.014
Liu, D., Zhao, Z., Zhu, D.-C., Niu, Y., Depaolo, D. J., Harrison, T. M., et al. (2014). Postcollisional potassic and ultrapotassic rocks in southern Tibet: Mantle and crustal origins in response to India–Asia collision and convergence. *Geochimica et Cosmochimica Acta*, *143*, 207–231. https://doi.org/10.1016/j.gca.2014.03.031
Magott, R., Fabbri, O., & Fournier, M. (2016). Subduction zone intermediate-depth seismicity: Insights from the structural analysis of Alpine high-pressure ophiolite-hosted pseudotachylyte (Corsica, France). *Journal of Structural Geology*, *87*, 95–114. https://doi.org/10.1016/j.jsg.2016.04.002
Maruyama, S., Liou, J. G., & Terebayashi, M. (1996). Blueschists and eclogites of the world and their exhumation. *International Geology Review*, *38*(6), 485–594. https://doi.org/10.1080/00206819709465347
Maury, J., Ide, S., Cruz-Atienza, V. M., Kostoglodov, V., González-Molina, G., & Pérez-Campos, X. (2016). Comparative study of tectonic tremor locations: Characterization of slow earthquakes in Guerrero, Mexico. *Journal of Geophysical Research: Solid Earth*, *121*(7), 5136–5151. https://doi.org/10.1002/2016JB013027
McCaffrey, R. (2008). Global frequency of magnitude 9 earthquakes. *Geology*, *36*(3), 263. https://doi.org/10.1130/g24402a.1
McCaffrey, R., Molnar, P., Roecker, S. W., & Joyodiwiryo, Y. S. (1985). Microearthquake seismicity and fault plane solutions related to arc-continent collision in the Eastern Sunda Arc, Indonesia. *Journal of Geophysical Research*, *90*(B6), 4511–4528. https://doi.org/10.1029/JB090iB06p04511
Menant, A., Angiboust, S., Monié, P., Oncken, O., & Guigner, J.-M. (2018). Brittle deformation during Alpine basal accretion and the origin of seismicity nests above the subduction interface. *Earth and Planetary Science Letters*, *487*, 84–93. https://doi.org/10.1016/j.epsl.2018.01.029
Miller, N. C., & Behn, M. D. (2012). Timescales for the growth of sediment diapirs in subduction zones: Sediment diapirs in subduction zones. *Geophysical Journal International*, *190*(3), 1361–1377. https://doi.org/10.1111/j.1365-246X.2012.05565.x
Miyashiro, A. (1972). Metamorphism and related magmatism in plate tectonics. *American Journal of Science*, *272*(7), 629–656. https://doi.org/10.2475/ajs.272.7.629
Miyashiro, A. (1973). Paired and unpaired metamorphic belts. *Tectonophysics*, *17*(3), 241–254. https://doi.org/10.1016/0040-1951(73)90005-x
Molnar, P. (1979). Earthquake recurrence intervals and plate tectonics. *Bulletin of the Seismological Society of America*, *69*(1), 115–133. https://doi.org/10.1785/bssa0690010115
Molnar, P., & England, P. (1990). Temperatures, heat flux, and frictional stress near major thrust faults. *Journal of Geophysical Research*, *95*(B4), 4833–4856. https://doi.org/10.1029/jb095ib04p04833
Molnar, P., Houseman, G., & Conrad, C. (1998). Rayleigh–Taylor instability and convective thinning of mechanically thickened lithosphere: Effects of non-linear viscosity decreasing exponentially with depth and of horizontal shortening of the layer. *Geophysical Journal International*, *133*(3), 568–584. https://doi.org/10.1046/j.1365-246x.1998.00510.x
Monié, P., & Agard, P. (2009). Coeval blueschist exhumation along thousands of kilometers: Implications for subduction channel processes. *Geochemistry, Geophysics, Geosystems*, *10*(7), Q07002. https://doi.org/10.1029/2009gc002428
Nakajima, J., Hada, S., Hayami, E., Uchida, N., Hasegawa, A., Yoshioka, S., et al. (2013). Seismic attenuation beneath northeastern Japan: Constraints on mantle dynamics and arc magmatism. *Journal of Geophysical Research: Solid Earth*, *118*(11), 5838–5855. https://doi.org/10.1002/2013jb010388
Obara, K. (2011). Characteristics and interactions between non-volcanic tremor and related slow earthquakes in the Nankai subduction zone, southwest Japan. *Journal of Geodynamics*, *52*(3–4), 229–248. https://doi.org/10.1016/j.jog.2011.04.002
O'Brien, T. M., & Grove, M. (2022). Subduction accretion, thermal overprinting, and exhumation of high-pressure/low-temperature metasedimentary rocks of the south-central Brooks Range. *International Geology Review*, *64*(1), 119–149. https://doi.org/10.1080/00206814.2020.1841684
Okamoto, S., Kimura, G., Yamaguchi, A., Yamaguchi, H., & Kusuba, Y. (2007). Generation depth of the pseudotachylyte from an out-of-sequence thrust in Accretionary prism – Geothermobarometric evidence. *Scientific Drilling*, Special Issue, 47–50. https://doi.org/10.5194/sd-SpecialIssue-47-2007
Oxburgh, E. R., & Turcotte, D. L. (1971). Origin of paired metamorphic belts and crustal dilation in island arc regions. *Journal of Geophysical Research*, *76*(5), 1315–1327. https://doi.org/10.1029/jb076i005p01315
Palin, R. M., Weller, O. M., Waters, D. J., & Dyck, B. (2016). Quantifying geological uncertainty in metamorphic phase equilibria modelling; a Monte Carlo assessment and implications for tectonic interpretations. *Geoscience Frontiers*, *7*(4), 591–607. https://doi.org/10.1016/j.gsf.2015.08.005
Paola, C., & Leeder, M. (2011). Simplicity versus complexity. *Nature*, *469*(7328), 38–39. https://doi.org/10.1038/469038a
Parsons, B., & Sclater, J. G. (1977). An analysis of the variation of ocean floor bathymetry and heat flow with age. *Journal of Geophysical Research*, *82*(5), 802–827. https://doi.org/10.1029/jb082i005p00803
Patzig, R., Shapiro, S., Asch, G., Giese, P., & Wigger, P. (2002). Seismogenic plane of the northern Andean Subduction Zone from aftershocks of the Antofagasta (Chile) 1995 earthquake. *Geophysical Research Letters*, *29*(8), 1264–105-4. https://doi.org/10.1029/2001gl013244
Peacock, S. M. (1990). Fluid processes in subduction zones. *Science*, *248*(4953), 329–337. https://doi.org/10.1126/science.248.4953.329
Peacock, S. M. (1992). Blueschist-facies metamorphism, shear heating, and P-T-t paths in subduction shear zones. *Journal of Geophysical Research*, *97*(B12), 17693–17707. https://doi.org/10.1029/92jb01768
Peacock, S. M. (1996). Thermal and petrologic structure of subduction zones. In G. E. Bebout (Ed.), *Subduction top to bottom*, *Geophysical Monograph Series* (pp. 105–111). American Geophysical Union.
Peng, Z., & Gomberg, J. (2010). An integrated perspective of the continuum between earthquakes and slow-slip phenomena. *Nature Geoscience*, *3*(9), 599–607. https://doi.org/10.1038/ngeo940
Penniston-Dorland, S. C., Kohn, M. J., & Manning, C. E. (2015). The global range of subduction zone thermal structures from exhumed blueschists and eclogites: Rocks are hotter than models. *Earth and Planetary Science Letters*, *428*, 243–254. https://doi.org/10.1016/j.epsl.2015.07.031
Pittarello, L., Levi, N., Wegner, W., & Stehlik, H. (2022). The pseudotachylytes at the base of the Silvretta Nappe: A newly discovered recent generation and the tectonomometamophic evolution of the Nappe. *Tectonophysics*, *822*, 229185. https://doi.org/10.1016/j.tecto.2021.229185
Plank, T., & Langmuir, C. (1993). Tracing trace elements from sediment input to volcanic output at subduction zones. *Nature*, *362*(6422), 739–743. https://doi.org/10.1038/362739a0

Platt, J. (1993). Mechanics of oblique convergence. *Journal of Geophysical Research*, *98*(B9), 16239–16256. https://doi.org/10.1029/93jb00888
Platt, J. P. (1987). The uplift of high-pressure low-temperature metamorphic rocks. *Philosophical Transactions of the Royal Society A: Mathematical, Physical & Engineering Sciences*, *321*, 87–103.
Platt, J. P. (2015). Rheology of two-phase systems: A microphysical and observational approach. *Journal of Structural Geology*, *77*, 213–227. https://doi.org/10.1016/j.jsg.2015.05.003
Plunder, A., Agard, P., Chopin, C., Pourteau, A., & Okay, A. I. (2015). Accretion, underplating and exhumation along a subduction interface: From subduction initiation to continental subduction (Tavşanlı zone, W. Turkey). *Lithos*, *226*, 233–254. https://doi.org/10.1016/j.lithos.2015.01.007
Powell, R., & Holland, T. (1988). An internally consistent dataset with uncertainties and correlations: 3. Applications to geobarometry, worked examples and a computer program. *Journal of Metamorphic Geology*, *6*(2), 173–204. https://doi.org/10.1111/j.1525-1314.1988.tb00415.x
Powell, R., & Holland, T. (1994). Optimal geothermometry and geobarometry. *American Mineralogist*, *79*, 120–133.
Rad, G. F., Droop, G., Amini, S., & Moazzen, M. (2005). Eclogites and blueschists of the Sistan Suture Zone, eastern Iran: A comparison of P–T histories from a subduction mélange. *Lithos*, *84*(1–2), 1–24. https://doi.org/10.1016/j.lithos.2005.01.007
Reinecke, T. (1991). Very-high-pressure metamorphism and uplift of coesite-bearing metasediments from the Zermatt-Saas zone, Western Alps. *European Journal of Mineralogy*, *3*(1), 7–18. https://doi.org/10.1127/ejm/3/1/0007
Reinecke, T. (1998). Prograde high-to ultrahigh-pressure metamorphism and exhumation of oceanic sediments at Lago di Cignana, Zermatt-Saas Zone, western Alps. *Lithos*, *42*(3–4), 147–189. https://doi.org/10.1016/s0024-4937(97)00041-8
Rice, J. R. (2006). Heating and weakening of faults during earthquake slip. *Journal of Geophysical Research*, *111*(B5), 29. https://doi.org/10.1029/2005jb004006
Ring, U., Pantazides, H., Glodny, J., & Skelton, A. (2020). Forced return flow deep in the subduction channel, Syros, Greece. *Tectonics*, *39*(1), e2019TC005768. https://doi.org/10.1029/2019TC005768
Rong, Y., Jackson, D. D., Magistrale, H., & Goldfinger, C. (2014). Magnitude limits of subduction zone earthquakes. *Bulletin of the Seismological Society of America*, *104*(5), 2359–2377. https://doi.org/10.1785/0120130287
Rowe, C. D., & Griffith, W. A. (2015). Do faults preserve a record of seismic slip: A second opinion. *Journal of Structural Geology*, *78*, 1–26. https://doi.org/10.1016/j.jsg.2015.06.006
Rowe, C. D., Meneghini, F., & Moore, J. C. (2011). Textural record of the seismic cycle: Strain-rate variation in an ancient subduction thrust. *Geological Society London Special Publications*, *359*(1), 77–95. https://doi.org/10.1144/sp359.5
Rubatto, D., Regis, D., Hermann, J., Boston, K., Engi, M., Beltrando, M., & McAlpine, S. R. B. (2011). Yo-yo subduction recorded by accessory minerals in the Italian Western Alps. *Nature Geoscience*, *4*(5), 338–342. https://doi.org/10.1038/ngeo1124
Rupke, L. (2004). Serpentine and the subduction zone water cycle. *Earth and Planetary Science Letters*, *223*(1–2), 17–34. https://doi.org/10.1016/j.epsl.2004.04.018
Rybacki, E., Konrad, K., Renner, J., Wachmann, M., Stöckhert, B., & Rummel, F. (2003). Experimental deformation of synthetic aragonite marble. *Journal of Geophysical Research*, *108*(B3). https://doi.org/10.1029/2001JB000694
Rychert, C. A., Fischer, K. M., Abers, G. A., Plank, T., Syracuse, E., Protti, J. M., et al. (2008). Strong along-arc variations in attenuation in the mantle wedge beneath Costa Rica and Nicaragua: Attenuation beneath Nicaragua and Costa Rica. *Geochemistry, Geophysics, Geosystems*, *9*(10), Q10S10. https://doi.org/10.1029/2008GC002040
Saffer, D. M., & Wallace, L. M. (2015). The frictional, hydrologic, metamorphic and thermal habitat of shallow slow earthquakes. *Nature Geoscience*, *8*, 594–600. https://doi.org/10.1038/ngeo2490
Scholl, D., & von Huene, R. (2007). Crustal recycling at modern subduction zones applied to the past: Issues of growth and preservation of continental basement crust, mantle geochemistry, and supercontinent reconstruction. In R. D. Hatcher, M. P. Carlson, J. H. McBride, & J. R. M. Catalán (Eds.), *4D framework of continental crust*. *Geological Society of America Memoirs* (Vol. *200*, pp. 9–32). https://doi.org/10.1130/2007.1200(02)
Scholz, C. H., & Campos, J. (2012). The seismic coupling of subduction zones revisited. *Journal of Geophysical Research*, *117*(B5), B05310. https://doi.org/10.1029/2011jb009003
Schurr, B., Asch, G., Rietbrock, A., Trumbull, R., & Haberland, C. (2003). Complex patterns of fluid and melt transport in the central Andean subduction zone revealed by attenuation tomography. *Earth and Planetary Science Letters*, *215*(1–2), 105–119. https://doi.org/10.1016/s0012-821x(03)00441-2
Schurr, B., Rietbrock, A., Asch, G., Kind, R., & Oncken, O. (2006). Evidence for lithospheric detachment in the central Andes from local earthquake tomography. *Tectonophysics*, *415*(1–4), 203–223. https://doi.org/10.1016/j.tecto.2005.12.007
Schwartz, S. Y., & Rokosky, J. M. (2007). Slow slip events and seismic tremor at circum-Pacific subduction zones. *Reviews of Geophysics*, *45*(3), RG3004. https://doi.org/10.1029/2006rg000208
Searle, M., Waters, D., Martin, H., & Rex, D. (1994). Structure and metamorphism of blueschist–eclogite facies rocks from the northeastern Oman Mountains. *Journal of the Geological Society*, *151*(3), 555–576. https://doi.org/10.1144/gsjgs.151.3.0555
Şengün, F., Davis, P., Tunç, İ., & Yiğitbaş, E. (2012). Petrology and geochemistry of eclogites from the Biga Peninsula, Northwest Turkey. *Geodinamica Acta*, *25*(3–4), 248–266. https://doi.org/10.1080/09853111.2013.858954
Shreve, R. L., & Cloos, M. (1986). Dynamics of sediment subduction, melange formation, and prism accretion. *Journal of Geophysical Research*, *91*(B10), 10229–10245. https://doi.org/10.1029/jb091ib10p10229
Sibson, R. H. (2003). Thickness of the seismic slip zone. *Bulletin of the Seismological Society of America*, *93*(3), 1169–1178. https://doi.org/10.1785/0120020061
Sibson, R. H., & Toy, V. G. (2006). The habitat of fault-generated pseudotachylyte: Presence vs. absence of friction-melt. In *Earthquakes: Radiated energy and the physics of faulting* (pp. 153–166). American Geophysical Union.
Smye, A. J., Bickle, M. J., Holland, T. J., Parrish, R. R., & Condon, D. J. (2011). Rapid formation and exhumation of the youngest alpine eclogites: A thermal conundrum to barrovian metamorphism. *Earth and Planetary Science Letters*, *306*(3–4), 193–204. https://doi.org/10.1016/j.epsl.2011.03.037
Smye, A. J., & England, P. C. (2022). Metamorphism and deformation on subduction interfaces: 2. Petrological and tectonic implications. *Geochemistry, Geophysics, Geosystems*, *23*, e2022GC010645. https://doi.org/10.1029/2022GC010645
Smye, A. J., Greenwood, L. V., & Holland, T. J. B. (2010). Garnet-chloritoid-kyanite assemblages: Eclogite facies indicators of subduction constraints in orogenic belts. *Journal of Metamorphic Geology*, *28*(7), 753–768. https://doi.org/10.1111/j.1525-1314.2010.00889.x
Smye, A. J., Seman, S. M., Scambelluri, M., Starr, P. G., & Federico, L. (2021). Exhumation dynamics of high-pressure metamorphic rocks from the Voltri Unit, Western Alps: Constraints from phengite Rb–Sr geochronology. *Contributions to Mineralogy and Petrology*, *176*(2), 1–24. https://doi.org/10.1007/s00410-020-01767-0

Song, T.-R. A., Helmberger, D. V., Brudzinski, M. R., Clayton, R. W., Davis, P., Perez-Campos, X., & Singh, S. K. (2009). Subducting slab ultra-slow velocity layer coincident with silent earthquakes in southern Mexico. *Science*, *324*(5926), 502–506. https://doi.org/10.1126/science.1167595

Stachnik, J. C., Abers, G. A., & Christensen, D. H. (2004). Seismic attenuation and mantle wedge temperatures in the Alaska subduction zone. *Journal of Geophysical Research*, *109*(B10), B10304. https://doi.org/10.1029/2004JB003018

Starr, P. G., Broadwell, K. S., Dragovic, B., Scambelluri, M., Haws, A. A., Caddick, M. J., et al. (2020). The subduction and exhumation history of the Voltri Ophiolite, Italy: Evaluating exhumation mechanisms for high-pressure metamorphic massifs. *Lithos*, *376*, 105767. https://doi.org/10.1016/j.lithos.2020.105767

Stein, S., & Okal, E. A. (2007). Ultralong period seismic study of the December 2004 Indian Ocean earthquake and implications for regional tectonics and the subduction process. *Bulletin of the Seismological Society of America*, *97*(1A), S279–S295. https://doi.org/10.1785/0120050617

Syracuse, E. M., Keken, P. E. V., & Abers, G. A. (2010). The global range of subduction zone thermal models. *Physics of the Earth and Planetary Interiors*, *183*(1–2), 73–90. https://doi.org/10.1016/j.pepi.2010.02.004

Tamblyn, R., Hand, M., Morrissey, L., Zack, T., Phillips, G., & Och, D. (2020). Resubduction of lawsonite eclogite within a serpentinite-filled subduction channel. *Contributions to Mineralogy and Petrology*, *175*(8), 74. https://doi.org/10.1007/s00410-020-01712-1

Tera, F., Brown, L., Morris, J., Sacks, I. S., Klein, J., & Middleton, R. (1986). Sediment incorporation in island-arc magmas: Inferences from ^{10}Be. *Geochimica et Cosmochimica Acta*, *50*(4), 535–550. https://doi.org/10.1016/0016-7037(86)90103-1

Tsujimori, T., & Ernst, W. (2013). Lawsonite blueschists and lawsonite eclogites as proxies for palaeo-subduction zone processes: A review. *Journal of Metamorphic Geology*, *32*(5), 437–454. https://doi.org/10.1111/jmg.12057

Turcotte, D. L., & Schubert, G. (1973). Frictional heating of descending lithosphere. *Journal of Geophysical Research*, *78*(26), 5876–5886. https://doi.org/10.1029/jb078i026p05876

Turcotte, D. L., & Schubert, G. (2014). *Geodynamics* (3rd ed.). Cambridge University Press.

Turner, S. J., & Langmuir, C. H. (2022). A quantitative framework for global variations in arc geochemistry. *Earth and Planetary Science Letters*, *584*, 117411. https://doi.org/10.1016/j.epsl.2022.117411

Ukar, E., & Cloos, M. (2013). Actinolitic rinds on low-T mafic blueschist blocks in the Franciscan shale-matrix mélange near San Simeon: Implications for metasomatism and tectonic history. *Earth and Planetary Science Letters*, *377*, 155–168. https://doi.org/10.1016/j.epsl.2013.06.038

van Keken, P. E., Wada, I., Abers, G. A., Hacker, B. R., & Wang, K. (2018). Mafic high-pressure rocks are preferentially exhumed from warm subduction settings. *Geochemistry, Geophysics, Geosystems*, *19*(9), 2934–2961. https://doi.org/10.1029/2018gc007624

van Keken, P. E., Wada, I., Sime, N., & Abers, G. A. (2019). Thermal structure of the Forearc in subduction zones: A comparison of methodologies. *Geochemistry, Geophysics, Geosystems*, *20*(7), 3268–3288. https://doi.org/10.1029/2019GC008334

Ventouzi, C., Papazachos, C., Hatzidimitriou, P., Papaioannou, C., & EGELADOS Working Group. (2018). Anelastic P- and S- upper mantle attenuation tomography of the southern Aegean Sea subduction area (Hellenic Arc) using intermediate-depth earthquake data. *Geophysical Journal International*, *215*(1), 635–658. https://doi.org/10.1093/gji/ggy292

Vitale, S., Fedele, L., Tramparulo, F. D., & Prinzi, E. P. (2019). Fault rocks within the blueschist metabasalts of the Diamante–Terranova unit (southern Italy): Potential fossil record of intermediate-depth subduction earthquakes. *Geological Magazine*, *156*(10), 1771–1782. https://doi.org/10.1017/S0016756819000062

Vitale Brovarone, A., & Agard, P. (2013). True metamorphic isograds or tectonically sliced metamorphic sequence? New high-spatial resolution petrological data for the New Caledonia case study. *Contributions to Mineralogy and Petrology*, *166*(2), 451–469. https://doi.org/10.1007/s00410-013-0885-2

von Huene, R., & Scholl, D. (1991). Observations at convergent margins concerning sediment subduction, subduction erosion, and the growth of continental crust. *Reviews of Geophysics*, *29*(3), 279–316. https://doi.org/10.1029/91rg00969

Wada, I., & Wang, K. (2009). Common depth of slab-mantle decoupling: Reconciling diversity and uniformity of subduction zones. *Geochemistry, Geophysics, Geosystems*, *10*, 1–36. https://doi.org/10.1029/2009gc002570

Wakabayashi, J. (2012). Subducted sedimentary serpentinite mélanges: Record of multiple burial–exhumation cycles and subduction erosion. *Tectonophysics*, *568*, 230–247. https://doi.org/10.1016/j.tecto.2011.11.006

Wakabayashi, J., & Dilek, Y. (2011). Mélanges of the franciscan complex, California: Diverse structural settings, evidence for sedimentary mixing, and their connection to subduction processes, mélanges: Processes of formation and societal significance. *Geological Society of America Special Paper*, *480*, 117–141.

Walther, J. V., & Orville, P. M. (1982). Volatile production and transport in regional metamorphism. *Contributions to Mineralogy and Petrology*, *79*(3), 252–257. https://doi.org/10.1007/bf00371516

Wang, K., & Dixon, T. (2004). "Coupling" semantics and science in earthquake research. *Eos, Transactions American Geophysical Union*, *85*(18), 180. https://doi.org/10.1029/2004eo180005

Wang, K., & Tréhu, A. M. (2016). Some outstanding issues in the study of great megathrust earthquakes—The Cascadia example. *Journal of Geodynamics*, *98*, 1–18. https://doi.org/10.1016/j.jog.2016.03.010

Waters, D. (1993). Geobarometry of phengite-bearing eclogites. *Terra Abstracts*, *5*, 410–411.

Wech, A. G. (2021). Cataloging tectonic tremor energy radiation in the Cascadia subduction zone. *Journal of Geophysical Research: Solid Earth*, *126*(10), e2021JB022523. https://doi.org/10.1029/2021JB022523

Wei, S. S., & Wiens, D. A. (2018). P-wave attenuation structure of the Lau back-arc basin and implications for mantle wedge processes. *Earth and Planetary Science Letters*, *502*, 187–199. https://doi.org/10.1016/j.epsl.2018.09.005

Wessel, P., Smith, W. H. F., Scharroo, R., Luis, J., & Wobbe, F. (2013). Generic Mapping Tools: Improved version released. *Eos, Transactions American Geophysical Union*, *94*(45), 409–410. https://doi.org/10.1002/2013eo450001

Whitney, D. L., & Davis, P. B. (2006). Why is lawsonite eclogite so rare? Metamorphism and preservation of lawsonite eclogite, sivrihisar, Turkey. *Geology*, *34*(6), 473–476. https://doi.org/10.1130/g22259.1

Xia, H., & Platt, J. P. (2017). Structural and rheological evolution of the Laramide subduction channel in southern California. *Solid Earth*, *8*(2), 379–403. https://doi.org/10.5194/se-8-379-2017

Yuen, D. A., Fleitout, L., Schubert, G., & Froidevaux, C. (1978). Shear deformation zones along major transform faults and subducting slabs. *Geophysical Journal International*, *54*(1), 93–119. https://doi.org/10.1111/j.1365-246X.1978.tb06758.x